DESY 09-162 ISSN 0418-9833
February 2010

Jet Production in ep Collisions at Low Q^2 and Determination of α_s

H1 Collaboration

Abstract

The production of jets is studied in deep-inelastic e^+p scattering at low negative four momentum transfer squared $5 < Q^2 < 100$ GeV^2 and at inelasticity $0.2 < y < 0.7$ using data recorded by the H1 detector at HERA in the years 1999 and 2000, corresponding to an integrated luminosity of $43.5\,\mathrm{pb}^{-1}$. Inclusive jet, 2-jet and 3-jet cross sections as well as the ratio of 3-jet to 2-jet cross sections are measured as a function of Q^2 and jet transverse momentum. The 2-jet cross section is also measured as a function of the proton momentum fraction ξ. The measurements are well described by perturbative quantum chromodynamics at next-to-leading order corrected for hadronisation effects and are subsequently used to extract the strong coupling α_s.

Accepted by *Eur.Phys.J.C*

F.D. Aaron[5,49], M. Aldaya Martin[11], C. Alexa[5], V. Andreev[25], B. Antunovic[11], S. Backovic[30], A. Baghdasaryan[38], E. Barrelet[29], W. Bartel[11], K. Begzsuren[35], A. Belousov[25], J.C. Bizot[27], V. Boudry[28], I. Bozovic-Jelisavcic[2], J. Bracinik[3], G. Brandt[11], M. Brinkmann[12], V. Brisson[27], D. Bruncko[16], A. Bunyatyan[13,38], G. Buschhorn[26], L. Bystritskaya[24], A.J. Campbell[11], K.B. Cantun Avila[22], K. Cerny[32], V. Cerny[16,47], V. Chekelian[26], A. Cholewa[11], J.G. Contreras[22], J.A. Coughlan[6], G. Cozzika[10], J. Cvach[31], J.B. Dainton[18], K. Daum[37,43], M. Deák[11], B. Delcourt[27], J. Delvax[4], E.A. De Wolf[4], C. Diaconu[21], V. Dodonov[13], A. Dossanov[26], A. Dubak[30,46], G. Eckerlin[11], V. Efremenko[24], S. Egli[36], A. Eliseev[25], E. Elsen[11], A. Falkiewicz[7], L. Favart[4], A. Fedotov[24], R. Felst[11], J. Feltesse[10,48], J. Ferencei[16], D.-J. Fischer[11], M. Fleischer[11], A. Fomenko[25], E. Gabathuler[18], J. Gayler[11], S. Ghazaryan[11], A. Glazov[11], I. Glushkov[39], L. Goerlich[7], N. Gogitidze[25], M. Gouzevitch[11], C. Grab[40], T. Greenshaw[18], B.R. Grell[11], G. Grindhammer[26], S. Habib[12], D. Haidt[11], C. Helebrant[11], R.C.W. Henderson[17], E. Hennekemper[15], H. Henschel[39], M. Herbst[15], G. Herrera[23], M. Hildebrandt[36], K.H. Hiller[39], D. Hoffmann[21], R. Horisberger[36], T. Hreus[4,44], M. Jacquet[27], X. Janssen[4], L. Jönsson[20], A.W. Jung[15], H. Jung[11], M. Kapichine[9], J. Katzy[11], I.R. Kenyon[3], C. Kiesling[26], M. Klein[18], C. Kleinwort[11], T. Kluge[18], A. Knutsson[11], R. Kogler[26], E. Kosior[11], P. Kostka[39], M. Kraemer[11], K. Krastev[11], J. Kretzschmar[18], A. Kropivnitskaya[24], K. Krüger[15], K. Kutak[11], M.P.J. Landon[19], W. Lange[39], G. Laštovička-Medin[30], P. Laycock[18], A. Lebedev[25], V. Lendermann[15], S. Levonian[11], G. Li[27], K. Lipka[11], A. Liptaj[26], B. List[12], J. List[11], N. Loktionova[25], R. Lopez-Fernandez[23], V. Lubimov[24], A. Makankine[9], E. Malinovski[25], P. Marage[4], Ll. Marti[11], H.-U. Martyn[1], S.J. Maxfield[18], A. Mehta[18], A.B. Meyer[11], H. Meyer[11], H. Meyer[37], J. Meyer[11], S. Mikocki[7], I. Milcewicz-Mika[7], F. Moreau[28], A. Morozov[9], J.V. Morris[6], M.U. Mozer[4], M. Mudrinic[2], K. Müller[41], P. Murín[16,44], Th. Naumann[39], P.R. Newman[3], C. Niebuhr[11], A. Nikiforov[11], D. Nikitin[9], G. Nowak[7], K. Nowak[41], J.E. Olsson[11], S. Osman[20], D. Ozerov[24], V. Palichik[9], I. Panagoulias[l,11,42], M. Pandurovic[2], Th. Papadopoulou[l,11,42], C. Pascaud[27], G.D. Patel[18], O. Pejchal[32], E. Perez[10,45], A. Petrukhin[24], I. Picuric[30], S. Piec[39], D. Pitzl[11], R. Plačakytė[11], B. Pokorny[12], R. Polifka[32], B. Povh[13], V. Radescu[11], A.J. Rahmat[18], N. Raicevic[30], A. Raspiareza[26], T. Ravdandorj[35], P. Reimer[31], E. Rizvi[19], P. Robmann[41], B. Roland[4], R. Roosen[4], A. Rostovtsev[24], M. Rotaru[5], J.E. Ruiz Tabasco[22], S. Rusakov[25], D. Šálek[32], D.P.C. Sankey[6], M. Sauter[14], E. Sauvan[21], S. Schmitt[11], L. Schoeffel[10], A. Schöning[14], H.-C. Schultz-Coulon[15], F. Sefkow[11], R.N. Shaw-West[3], L.N. Shtarkov[25], S. Shushkevich[26], T. Sloan[17], I. Smiljanic[2], Y. Soloviev[25], P. Sopicki[7], D. South[8], V. Spaskov[9], A. Specka[28], Z. Staykova[11], M. Steder[11], B. Stella[33], G. Stoicea[5], U. Straumann[41], D. Sunar[4], T. Sykora[4], V. Tchoulakov[9], G. Thompson[19], P.D. Thompson[3], T. Toll[12], F. Tomasz[16], T.H. Tran[27], D. Traynor[19], T.N. Trinh[21], P. Truöl[41], I. Tsakov[34], B. Tseepeldorj[35,50], J. Turnau[7], K. Urban[15], A. Valkárová[32], C. Vallée[21], P. Van Mechelen[4], A. Vargas Trevino[11], Y. Vazdik[25], S. Vinokurova[11], V. Volchinski[38], M. von den Driesch[11], D. Wegener[8], Ch. Wissing[11], E. Wünsch[11], J. Žáček[32], J. Zálešák[31], Z. Zhang[27], A. Zhokin[24], T. Zimmermann[40], H. Zohrabyan[38], and F. Zomer[27]

[1] *I. Physikalisches Institut der RWTH, Aachen, Germany*
[2] *Vinca Institute of Nuclear Sciences, Belgrade, Serbia*
[3] *School of Physics and Astronomy, University of Birmingham, Birmingham, UK[b]*
[4] *Inter-University Institute for High Energies ULB-VUB, Brussels; Universiteit Antwerpen, Antwerpen; Belgium[c]*
[5] *National Institute for Physics and Nuclear Engineering (NIPNE) , Bucharest, Romania*
[6] *Rutherford Appleton Laboratory, Chilton, Didcot, UK[b]*
[7] *Institute for Nuclear Physics, Cracow, Poland[d]*
[8] *Institut für Physik, TU Dortmund, Dortmund, Germany[a]*

[9] *Joint Institute for Nuclear Research, Dubna, Russia*
[10] *CEA, DSM/Irfu, CE-Saclay, Gif-sur-Yvette, France*
[11] *DESY, Hamburg, Germany*
[12] *Institut für Experimentalphysik, Universität Hamburg, Hamburg, Germany*[a]
[13] *Max-Planck-Institut für Kernphysik, Heidelberg, Germany*
[14] *Physikalisches Institut, Universität Heidelberg, Heidelberg, Germany*[a]
[15] *Kirchhoff-Institut für Physik, Universität Heidelberg, Heidelberg, Germany*[a]
[16] *Institute of Experimental Physics, Slovak Academy of Sciences, Košice, Slovak Republic*[f]
[17] *Department of Physics, University of Lancaster, Lancaster, UK*[b]
[18] *Department of Physics, University of Liverpool, Liverpool, UK*[b]
[19] *Queen Mary and Westfield College, London, UK*[b]
[20] *Physics Department, University of Lund, Lund, Sweden*[g]
[21] *CPPM, CNRS/IN2P3 - Univ. Mediterranee, Marseille, France*
[22] *Departamento de Fisica Aplicada, CINVESTAV, Mérida, Yucatán, Mexico*[j]
[23] *Departamento de Fisica, CINVESTAV, México City, Mexico*[j]
[24] *Institute for Theoretical and Experimental Physics, Moscow, Russia*[k]
[25] *Lebedev Physical Institute, Moscow, Russia*[e]
[26] *Max-Planck-Institut für Physik, München, Germany*
[27] *LAL, Univ. Paris-Sud, CNRS/IN2P3, Orsay, France*
[28] *LLR, Ecole Polytechnique, CNRS/IN2P3, Palaiseau, France*
[29] *LPNHE, Universités Paris VI and VII, CNRS/IN2P3, Paris, France*
[30] *Faculty of Science, University of Montenegro, Podgorica, Montenegro*[e]
[31] *Institute of Physics, Academy of Sciences of the Czech Republic, Praha, Czech Republic*[h]
[32] *Faculty of Mathematics and Physics, Charles University, Praha, Czech Republic*[h]
[33] *Dipartimento di Fisica Università di Roma Tre and INFN Roma 3, Roma, Italy*
[34] *Institute for Nuclear Research and Nuclear Energy, Sofia, Bulgaria*[e]
[35] *Institute of Physics and Technology of the Mongolian Academy of Sciences , Ulaanbaatar, Mongolia*
[36] *Paul Scherrer Institut, Villigen, Switzerland*
[37] *Fachbereich C, Universität Wuppertal, Wuppertal, Germany*
[38] *Yerevan Physics Institute, Yerevan, Armenia*
[39] *DESY, Zeuthen, Germany*
[40] *Institut für Teilchenphysik, ETH, Zürich, Switzerland*[i]
[41] *Physik-Institut der Universität Zürich, Zürich, Switzerland*[i]

[42] *Also at Physics Department, National Technical University, Zografou Campus, GR-15773 Athens, Greece*
[43] *Also at Rechenzentrum, Universität Wuppertal, Wuppertal, Germany*
[44] *Also at University of P.J. Šafárik, Košice, Slovak Republic*
[45] *Also at CERN, Geneva, Switzerland*
[46] *Also at Max-Planck-Institut für Physik, München, Germany*
[47] *Also at Comenius University, Bratislava, Slovak Republic*
[48] *Also at DESY and University Hamburg, Helmholtz Humboldt Research Award*
[49] *Also at Faculty of Physics, University of Bucharest, Bucharest, Romania*
[50] *Also at Ulaanbaatar University, Ulaanbaatar, Mongolia*

[a] *Supported by the Bundesministerium für Bildung und Forschung, FRG, under contract numbers 05H09GUF, 05H09VHC, 05H09VHF, 05H16PEA*
[b] *Supported by the UK Science and Technology Facilities Council, and formerly by the UK Particle Physics and Astronomy Research Council*
[c] *Supported by FNRS-FWO-Vlaanderen, IISN-IIKW and IWT and by Interuniversity Attraction Poles Programme, Belgian Science Policy*
[d] *Partially Supported by Polish Ministry of Science and Higher Education, grant PBS/DESY/70/2006*
[e] *Supported by the Deutsche Forschungsgemeinschaft*
[f] *Supported by VEGA SR grant no. 2/7062/ 27*
[g] *Supported by the Swedish Natural Science Research Council*
[h] *Supported by the Ministry of Education of the Czech Republic under the projects LC527, INGO-1P05LA259 and MSM0021620859*
[i] *Supported by the Swiss National Science Foundation*
[j] *Supported by CONACYT, México, grant 48778-F*
[k] *Russian Foundation for Basic Research (RFBR), grant no 1329.2008.2*
[l] *This project is co-funded by the European Social Fund (75%) and National Resources (25%) - (EPEAEK II) - PYTHAGORAS II*

1 Introduction

Jet production in neutral current (NC) deep-inelastic scattering (DIS) at HERA provides an important testing ground for Quantum Chromodynamics (QCD). While inclusive DIS gives only indirect information on the strong coupling via scaling violations of the proton structure functions, the production of jets allows a direct measurement of α_s. The Born level contribution to DIS (Fig. 1(a)) generates no transverse momentum in the Breit frame, where the virtual boson and the proton collide head on [1]. Significant transverse momentum P_T in the Breit frame is produced at leading order (LO) in the strong coupling α_s by the QCD Compton (Fig. 1(b)) and boson-gluon fusion (Fig. 1(c)) processes. The latter dominates jet production for the range of the negative four momentum transfer squared of this analysis, $5 < Q^2 < 100\ \mathrm{GeV}^2$, and provides direct sensitivity to the gluon density function of the proton [2].

Analyses of inclusive and multi-jet production in DIS were previously performed at high Q^2 ($\gtrsim 100\ \mathrm{GeV}^2$) [2–5] and at low Q^2 ($\lesssim 100\ \mathrm{GeV}^2$) [2, 6, 7] by the H1 and ZEUS Collaborations at HERA. In this paper new measurements of the inclusive jet, 2-jet and 3-jet production cross sections, as well as the ratio of 3-jet to 2-jet cross sections, are presented as a function of Q^2 and the jet transverse momenta in the Breit frame, P_T, in the ranges $5 < Q^2 < 100\ \mathrm{GeV}^2$ and $P_T > 5\ \mathrm{GeV}$. The 2-jet cross section is also presented as a function of $\xi = x_{\mathrm{Bj}}(1 + M_{12}^2/Q^2)$, which in LO corresponds to the momentum fraction of the proton carried by the interacting parton (see Figs.1(b) and 1(c)). The variable x_{Bj} denotes the Bjorken scaling variable and M_{12} the invariant mass of the two jets of highest P_T. The data correspond to higher integrated luminosity and a higher centre-of-mass energy than in the previous H1 analyses at low Q^2 [2, 6]. The larger data set together with improved understanding of the hadronic energy measurement significantly reduces the total uncertainty of the cross section measurements. The results are compared with perturbative QCD predictions at next-to-leading order (NLO) corrected for hadronisation effects, and α_s is extracted from a fit of the predictions to the data. These measurements allow the running of the strong coupling to be tested down to the limits of the perturbative calculation. Together with the high Q^2 measurements [4] the data test the running of α_s in the range of renormalisation scale μ_r between about 6 and 70 GeV.

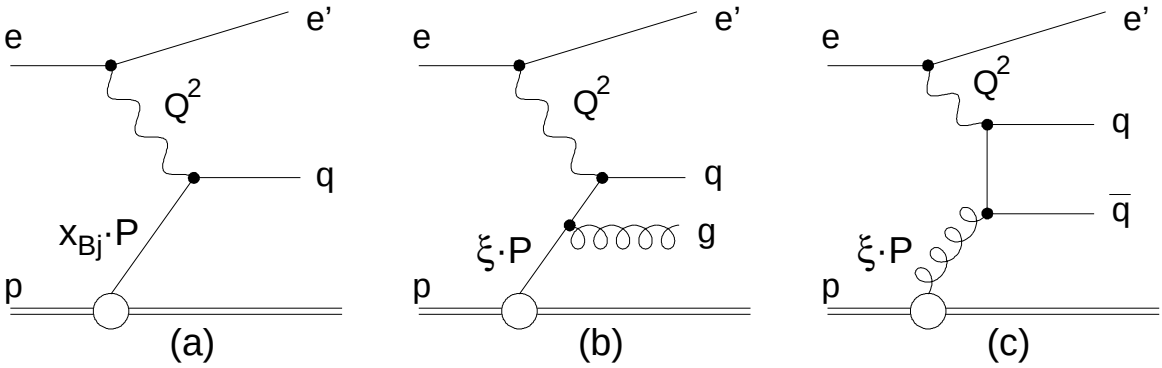

Figure 1: Deep-inelastic lepton-proton scattering at different orders in α_s: (a) Born contribution $\mathcal{O}(1)$ and $\mathcal{O}(\alpha_s)$ processes (b) QCD Compton scattering and (c) boson-gluon fusion.

2 Experimental Method

The data used for this analysis were recorded with H1 detector in the years 1999 and 2000, when HERA collided positrons of energy $E_e = 27.6$ GeV with protons of energy $E_p = 920$ GeV giving a centre-of-mass energy $\sqrt{s} = 319$ GeV. The corresponding integrated luminosity is 43.5 pb^{-1}.

2.1 The H1 detector

A detailed description of the H1 detector can be found in [8, 9]. Here, a brief account of the components most relevant to the present analysis is given. The origin of the H1 coordinate system is the nominal ep interaction point. The direction of the proton beam defines the positive z-axis (forward direction). The polar angle θ is measured with respect to this direction. The pseudorapidity is defined as $\eta = -\ln\tan(\theta/2)$.

In the central region ($20^\circ < \theta < 160^\circ$) the ep interaction region is surrounded by a two-layered silicon strip detector [10] and two large concentric drift chambers (CJCs), operated inside a 1.16 T solenoidal magnetic field. The trajectories of charged particles are measured in the central tracker with a transverse momentum resolution of $\sigma(p_T)/p_T = 0.006\, p_T/\text{GeV} \oplus 0.02$ [11]. Two additional drift chambers complement the CJCs by precisely measuring the z-coordinates of track segments and hence improve the determination of the polar angle. The central tracking detectors also provide triggering information based on track segments measured in the r-ϕ plane of the central jet chambers and on the z position of the event vertex obtained from the double layers of two multiwire proportional chambers (MWPCs). The forward tracking detector and the backward drift chamber (BDC) measure tracks of charged particles at smaller ($7^\circ < \theta < 25^\circ$) and larger ($155^\circ < \theta < 175^\circ$) polar angle than the central tracker, respectively.

A finely segmented electromagnetic and hadronic liquid argon (LAr) calorimeter [12] surrounds the tracking chambers. It has a polar angle coverage of $4^\circ < \theta < 154^\circ$ and full azimuthal acceptance. The energy resolution is $\sigma(E)/E = 0.12/\sqrt{E/\,\text{GeV}} \oplus 0.01$ for electromagnetic showers and $\sigma(E)/E = 0.5/\sqrt{E/\,\text{GeV}} \oplus 0.02$ for hadrons, as measured in test beams [13]. A lead-scintillating fibre spaghetti calorimeter (SpaCal) [9] covers the backward region $153^\circ < \theta < 178^\circ$. Its main purpose is the detection of scattered positrons. The energy resolution of the SpaCal for positrons is $\sigma(E)/E = 0.071/\sqrt{E/\,\text{GeV}} \oplus 0.01$.

The luminosity is measured via the Bethe-Heitler Bremsstrahlung process $ep \to ep\gamma$, the final state photon being detected in a crystal calorimeter at $z = -103$ m.

2.2 Event and jet selection

The data sample of this analysis was collected using a combination of triggers which require the scattered positron to be measured in the SpaCal, at least one high transverse momentum track ($p_T > 800$ MeV) to be reconstructed in the central tracking chambers and an event vertex to be identified by the MWPCs. The trigger efficiency is close to 100% for the whole analysis phase space as determined from the data using independent triggers as a reference.

The selection of NC DIS events is based on the identification of the scattered positron as the most energetic compact calorimetric deposit in the SpaCal with an energy $E'_e > 7.5\ \mathrm{GeV}$ and a polar angle $156^\circ < \theta'_e < 175^\circ$. The energy weighted radius of this cluster is required to be less than 4 cm, as expected for an electromagnetic shower. The cluster must be geometrically associated with a track candidate in the BDC. The z-coordinate of the primary event vertex is required to be within $\pm 35\ \mathrm{cm}$ of the nominal position of the interaction point.

The remaining clusters in the calorimeters and the charged tracks are combined to reconstruct the hadronic final state, using an algorithm which avoids double counting of energy [14, 15]. The total longitudinal energy balance, determined as the difference of the total energy E and the longitudinal component of the total momentum P_z, calculated from all detected particles including the scattered positron, must satisfy $45 < E - P_z < 65$ GeV. This requirement reduces contributions of DIS events with hard initial state photon radiation. For the latter events, the undetected photons propagating in the negative z direction lead to values of $E - P_z$ significantly lower than the expected value $2E_e = 55.2\,\mathrm{GeV}$. After this selection the contribution from photoproduction is negligible as estimated using Monte Carlo simulations.

The kinematic region covered by this analysis is defined by

$$5 < Q^2 < 100\ \mathrm{GeV}^2 \quad \text{and} \quad 0.2 < y < 0.7\,,$$

where $y = Q^2/(s \cdot x_{\mathrm{Bj}})$ quantifies the inelasticity of the interaction. These two variables are reconstructed from the four momenta of the scattered positron and the hadronic final state particles using the electron-sigma method [16].

Jet finding is performed in the Breit frame. The boost from the laboratory system is determined by Q^2, y and by the azimuthal angle of the scattered positron. Particles of the hadronic final state are clustered into jets using the inclusive k_T algorithm [17, 18] with the massless P_T recombination scheme and with the distance parameter in the $\eta - \phi$ plane $R_0 = 1$. The cut $-1 < \eta^{\mathrm{jet}}_{\mathrm{Lab}} < 2.5$, where $\eta^{\mathrm{jet}}_{\mathrm{Lab}}$ is the jet pseudorapidity in the laboratory frame, ensures that jets are contained within the acceptance of the LAr calorimeter. The transverse energy of jets in the Breit frame is required to be above 5 GeV. Jets are ordered by decreasing transverse momentum P_T in the Breit frame, which is identical to the transverse energy E_T for massless jets. The jet with highest P_T is referred to as the "leading jet".

Three jet samples are defined: the inclusive jet sample contains all jets which satisfy the jet selection criteria; the 2-jet and 3-jet samples contain events with at least 2 and 3 jets, respectively. In addition, to avoid regions of phase space where fixed order perturbation theory is not reliable [19], 2-jet events are accepted only if the invariant mass M_{12} of the two leading jets exceeds 18 GeV. The same requirement is applied for 3-jet events such that the 3-jet sample is a subset of the 2-jet sample.

The selection criteria are summarised in Table 1. The final inclusive jet sample contains 164522 events with 230140 jets. The 2-jet and 3-jet samples contain 31550 and 4879 events respectively.

2.3 Determination of the jet cross sections

In order to extract the jet cross sections at hadron level, the experimental data are corrected bin-by-bin for effects of limited detector acceptance and resolution and for QED radiation effects. The following leading order Monte Carlo event generators are used for the correction procedure: DJANGOH [20], which uses the Colour Dipole Model with QCD matrix element corrections as implemented in ARIADNE [21], and RAPGAP [22], based on QCD matrix elements matched with parton showers in leading log approximation. The effects of QED radiation are included using the HERACLES [23] program interfaced with RAPGAP and DJANGOH. In both Monte Carlo generators the hadronisation is modelled with Lund string fragmentation [24]. The generated events are passed through a GEANT3 [25] based simulation of the H1 apparatus and are reconstructed using the same program chain as for the data. Both the RAPGAP and DJANGOH simulations provide a good overall description of the shapes of all relevant data distributions. To further improve the agreement between Monte Carlo and data, a reweighting as a function of Q^2 and P_T of the leading jet is applied to the Monte Carlo events.

The bin dependent correction factors are determined from Monte Carlo simulations as the ratios of the cross sections obtained from particles at hadron level without QED radiation to the cross section calculated using reconstructed particles and including QED radiation effects. The mean values of the correction factors determined by RAPGAP and DJANGOH are used, and half of the difference is assigned as a model uncertainty. The typical value of these factors is between 1.2 and 1.4.

The binnings in Q^2, P_T and ξ used to measure the jet cross sections are given in Table 2. The bin purities, defined as the fraction of events reconstructed in a particular bin that originate from that bin on hadron level, is found to be typically 70% and larger than 50% in all analysis bins. The bin stabilities, defined as the fraction of events originated from a particular bin on hadron level that are reconstructed in that bin, is typically 60% and larger than 40% in all analysis bins.

2.4 Experimental uncertainties

Several sources of experimental uncertainties are considered. The systematic uncertainties of the jet cross sections are determined by propagating the corresponding estimated measurement errors through the full analysis:

- The relative uncertainty of the positron energy calibration is better than 1%. The absolute uncertainty of the positron polar angle is about 1 mrad. Uncertainties in the positron reconstruction affect the event kinematics and thus the boost to the Breit frame. This in turn leads to a relative error of up to 2% on the jet cross section for each of the two sources.

- The relative uncertainty on the energy of the reconstructed hadronic final state as well as of the jet energy is estimated to be 2%. It is dominated by the uncertainty of the hadronic energy scale of the LAr calorimeter. Two different calibration methods are used for jet transverse momentum below and above 10 GeV, respectively. The resulting uncertainty on the cross sections is typically in the range of 4% to 10%. The uncertainty of the SpaCal hadronic energy scale of 7% contributes less than 1% to the uncertainty of the cross section.

- The model dependence of the detector correction factors is estimated as described in section 2.3. It reflects the sensitivity of the detector simulation to the details of the model, especially the parton showering and its impact on the migration between adjacent bins in P_T. The model dependence is below 10% in most of the bins and typically 4%.
- The luminosity measurement uncertainty leads to an overall normalisation error of the jet cross sections of 1.5%.

The uncertainty of the luminosity measurement is assumed to be fully correlated between the bins. The remaining sources of systematics, namely the positron energy scale and polar angle, the hadronic final state energy scale and the model dependence are assumed to be equally shared between correlated and uncorrelated parts.

The dominant experimental uncertainties on the jet cross sections arise from the model dependence of the data correction and from the LAr hadronic energy scale uncertainty. The individual contributions are added in quadrature to obtain the total systematic uncertainty.

3 NLO QCD Calculations

Reliable quantitative predictions of jet cross sections in DIS require the perturbative calculations to be performed at least to NLO in the strong coupling. The NLO calculations are used for comparison to data and for the α_s extraction. By using the inclusive k_T jet algorithm, the observables in the present analysis are infrared and collinear safe. Application of this algorithm in the Breit frame allows the initial state singularities to be absorbed in the definition of the proton parton densities, as needed for the calculation of factorised jet cross sections [26].

Jet cross sections are predicted at the parton level using the NLOJET++ program [27] at NLO in the strong coupling using the same jet definition as in the data analysis. When comparing data and theory predictions the strong coupling is taken to be $\alpha_s(M_Z) = 0.118$ at the Z^0 boson mass and is evolved as a function of the renormalisation scale with two loop precision. No QED radiation is included in the calculations, but the running of the electromagnetic coupling with Q^2 is taken into account in the theoretical predictions. The calculations are performed in the $\overline{\text{MS}}$ scheme [28] for five massless quark flavours. The parton density functions (PDFs) of the proton are taken from the CTEQ6.5M set [29]. The factorisation scale μ_f and the renormalisation scale μ_r are taken to be $\sqrt{(Q^2 + P^2_{T,\,\text{obs}})/2}$ for the NLO predictions, with $P_{T,\text{obs}}$ denoting the P_T of the jet for inclusive jet cross sections and the average transverse momentum of the two leading jets $\langle P_T \rangle$ for the 2-jet and 3-jet cross sections. This choice of the scales is motivated by the presence of two hard scales in jet production in DIS, P_T and Q, the latter being smaller in most of the analysis bins. The calculations were also performed using $\mu_r = P_{T,\text{obs}}$. With this choice of renormalisation scale the NLO QCD prediction decreases by $10 - 20\%$ at lowest Q^2 and P_T and is disfavoured by the data.

Hadronisation corrections are calculated for each bin using Monte Carlo event generators DJANGOH and RAPGAP which implement different models for parton showering. These corrections are determined as the ratio of the cross section at hadron level to the cross section at the

parton level after parton showers. It was verified that the parton level jet cross sections obtained from DJANGOH and RAPGAP are in agreement with those from the NLO calculation within the systematic uncertainties considered here. The hadronisation correction factors are determined as the average of values obtained from DJANGOH and RAPGAP. Half of the difference is assigned as hadronisation uncertainty and included as a part of the theoretical uncertainty. For inclusive and 2-jet cross sections the hadronisation correction factors differ typically by less than 10% from unity and agree at the level of 2 to 5% between the two Monte Carlo simulations. For 3-jet cross sections, as well as for the ratios of 3-jet to 2-jet cross sections, the hadronisation correction factors differ from unity by about 20% with up to 10% difference between the two MC models.

The dominant theoretical uncertainty is related to the missing higher orders in the perturbative calculation, and is conventionally estimated by separately varying the scales μ_f and μ_r by factors in the arbitrary range 0.5 to 2. The contributions from the two scale variations are similar and are added in quadrature to obtain the total scale dependence uncertainty. The uncertainty originating from the PDFs is taken into account for the α_s extraction using the variations of the CTEQ6.5M set of parton densities.

4 Cross Section Measurements

In the following, the differential cross sections, corresponding to the phase space given in Table 1, are presented for inclusive jet, 2-jet and 3-jet production at hadron level. Ratios of 3-jet to 2-jet hadron level cross sections are also presented. The measurements are shown in Tables 3 to 9 and Figs. 2 to 8.

4.1 Inclusive jet cross section

The measured inclusive jet cross section, corrected for detector and radiative QED effects, is presented as a function of Q^2 and P_T of the jet, as single differential distributions in Figs. 2(a,b) and double differentially in Fig. 3. Each jet which satisfies the jet selection criteria described in section 2.2 enters these distributions.

The measurements are well described by NLO QCD predictions corrected for hadronisation effects as explained in section 3. The theoretical uncertainty, dominated by the scale variation, reaches 30% for the lowest Q^2 and P_T bins and decreases to 10% for the highest Q^2 and P_T values. The relative contribution of hadronisation corrections to this error is small. The PDF uncertainty is about 6% at the lowest Q^2 and P_T and decreases to 2% for the highest Q^2.

4.2 2-jet and 3-jet cross sections

The measured single differential cross sections for 2-jet and 3-jet production as functions of Q^2 and of the average transverse momentum of the two leading jets $\langle P_T \rangle$ are shown in Figs. 2(c,e)

and Figs. 2(d,f) and are well described by the NLO QCD calculations corrected for hadronisation. The relative uncertainties on the NLO QCD calculations of 2-jet, 3-jet and inclusive cross sections are all of similar size.

The double differential 2-jet cross sections are presented in seven Q^2 bins as functions of the variables $\langle P_T \rangle$ and ξ in Fig. 4 and Fig. 5 respectively. The 3-jet cross section is shown in four Q^2 bins as a function of $\langle P_T \rangle$ in Fig. 6. The NLO QCD calculation provides an overall good description of the measured distributions within the quoted theoretical and experimental uncertainties. Requirements in P_T and M_{12} suppress the cross section at low ξ where a rise is expected due to the increase of the gluon density.

The present results for the inclusive and the 2-jet cross sections were compared to the previous H1 results in [2] and [6], respectively. Taking into account the difference between proton beam energies and differences in the kinematic region studied, the results are found to be consistent with each other.

The 3-jet cross section normalised to the 2-jet cross section is presented in Fig. 7 for single differential and in Fig. 8 for double differential distributions. This observable benefits from cancellation of the normalisation uncertainties and reduction of the other systematic uncertainties by about 50%. It is described by the NLO cross section except for the lowest $\langle P_T \rangle$ bin, as seen in Fig. 7(b) and Fig. 8, and shows a reduced sensitivity to the renormalisation scale variation which is done simultaneously for 2-jet and 3-jet cross sections. The ratio shows no significant dependence on Q^2 (Fig. 7(a)), but increases with $\langle P_T \rangle$ (Figs. 7(b),8) mainly due to the increasing phase space.

5 Extraction of the Strong Coupling

The QCD predictions for jet production depend on α_s and on the PDFs of the proton. The strong coupling α_s is determined from the measured jet cross sections using the PDFs as obtained from inclusive DIS data and other measurements.

5.1 Data and QCD predictions

The α_s determination is performed from individual bins of the double differential inclusive jet cross section, $d^2\sigma/dQ^2dP_T$, and the 2-jet and 3-jet cross sections, $d^2\sigma/dQ^2d\langle P_T \rangle$. Only bins are used in which the size of the k-factor, defined as the ratio of the cross sections calculated in NLO and LO (both obtained with NLOJET++), is below 2.5. The other bins most likely are affected by slow convergence of perturbation series and exhibit a high scale dependence, up to 30% at NLO.

The requirement that the k-factor be less than 2.5 corresponds to removing all points with $P_{T,\mathrm{obs}} < 10$ GeV for $Q^2 < 20\ \mathrm{GeV}^2$ from the inclusive jet and the 2-jet cross sections and points with $10 < P_{\mathrm{T}} < 15$ GeV for $Q^2 < 10\ \mathrm{GeV}^2$ from the inclusive jet cross section [1]. In

[1]The bins removed from the α_s analysis also correspond to the energy regime which is close to the b-quark mass threshold, where the five flavour massless approximation used in NLOJET++ is not expected to be valid.

total, 62 cross sections measurements are used for α_s extraction: 22 inclusive jet, 24 2-jet and all 16 3-jet points.

QCD predictions of the jet cross sections are calculated as a function of $\alpha_s(\mu_r)$ with the FastNLO package [30] using the CTEQ6.5M proton PDFs and applying the hadronisation corrections as described in section 3.

5.2 The χ^2 definition

Measurements and theory predictions are used to calculate a $\chi^2(\alpha_s)$ with the Hessian method [31], where parameters representing the systematic shifts of detector related observables, described in section 2.4, are left free in the fit. The shifts found by the fit are consistent with the *a priori* estimated experimental uncertainties. Due to different calibration strategies for jets with P_T above and below 10 GeV, two different parameters are used for the hadronic final state energy scale for bins with $P_{T,\mathrm{obs}} < 10$ GeV and $P_{T,\mathrm{obs}} \geq 10$ GeV. The Hessian method used here takes into account correlations of experimental uncertainties and has also been used in global data analyses [31, 32] and in previous H1 publications [3, 33]. The statistical correlations among the different bins and different observables are treated as described in [4, 34]. The experimental uncertainty of α_s is defined by the change in α_s which gives an increase in χ^2 of one unit with respect to the minimal value.

5.3 Theory and PDF uncertainties

The theoretical uncertainty is estimated by the offset method as the difference between the value of α_s from the nominal fit to the value when the fit is repeated with independent variations of different sources of theoretical uncertainties as described in section 3. The resulting uncertainties due to the different sources are summed in quadrature. The up (or down) variations are applied simultaneously to all bins in the fit. The impact of hadronisation corrections and the factorisation scale uncertainty on α_s typically amounts to 1% to 2% for each source. The largest uncertainty, of typically 8%, corresponds to the accuracy of the NLO approximation to the jet cross section estimated by varying the renormalisation scale as described in section 3.

The uncertainty due to PDFs is estimated by propagating the CTEQ6.5M errors. The typical size of the resulting error is 2% for α_s determined from the inclusive jet or 2-jet cross sections and 1% when measured with the 3-jet cross sections. This uncertainty is twice as large as that estimated with the uncertainties given for the MSTW2008nlo90cl set [35] which in turn exceeds the difference between α_s values extracted with the central sets of CTEQ6.5M, CTEQ6.6M [36] and MSTW2008nlo.

The CTEQ6.5M PDF parameterisation was obtained assuming $\alpha_s(M_Z) = 0.118$. In order to test whether this value of $\alpha_s(M_Z)$ biases the results obtained using the nominal method presented above, a method, similar to the one used in [3], is employed using the PDFs from the CTEQ6.6 series, which were obtained assuming different values for $\alpha_s(M_Z)$. The cross section as a function of the strong coupling is interpolated with a polynomial and this interpolation is used to determine the best fit of the strong coupling to the data. The result obtained with this alternative fit method is found to be compatible, well inside one standard deviation of the experimental error, with the value determined by the nominal method. Hence there is no indication for a bias due to the value of the strong coupling assumed for the CTEQ6.5M PDFs.

5.4 Fit results

The fits of the strong coupling α_s are performed individually for each of the 62 cross section measurements as described in section 5.1. These measurements constrain the value of the strong coupling at the Z^0 mass, $\alpha_s(M_Z)$. As an example, $\alpha_s(M_Z)$ values determined from the inclusive jet cross section are shown in Fig. 9. Different $\alpha_s(M_Z)$ values agree within experimental errors. For each of the three observables and each Q^2 region, fits of $\alpha_s(M_Z)$ to all P_T or $\langle P_T \rangle$ bins in that region are performed. The fit results are evolved from M_Z to the average scale μ_r in the respective Q^2 regions, where the average renormalisation scale μ_r is calculated using NLO predictions. Figs. 10(a-c) show the obtained $\alpha_s(\mu_r)$ values for fits to inclusive, 2-jet and 3-jet cross-sections, respectively. Also shown in these figures are QCD predictions $\alpha_s(\mu_r)$, derived from common fits of $\alpha_s(M_Z)$ to all respective Q^2 and P_T or $\langle P_T \rangle$ bins. The results of these three common fits are summarised in Table 10. If the points with k-factor above 2.5 are also included, the $\alpha_s(M_Z)$ values obtained are changed by less than one standard deviation of the total experimental uncertainty. As the $\alpha_s(M_Z)$ measurements derived from inclusive, 2-jet or 3-jet observables agree within uncertainties in any of the Q^2 regions, they are combined within four Q^2 regions, taking into account statistical and experimental systematic correlations. These results, evolved from the scale M_Z to the average μ_r in each region, are shown in Fig. 11(a). As compared to the case of extracting α_s from only one variable, the experimental uncertainties are reduced significantly.

Finally, all 62 data points are used in a common fit of the strong coupling taking the correlations into account with a fit quality $\chi^2/\mathrm{ndf} = 49.8/61$:

$$\alpha_s(M_Z) = 0.1160 \pm 0.0014(exp.)^{+0.0093}_{-0.0077}(th.) \pm 0.0016(\mathrm{PDF}). \quad (1)$$

The experimental error on $\alpha_s(M_Z)$ measured with each observable typically amounts to 1.5%. The combination of different observables, even though partially correlated, gives rise to additional constraints on the strong coupling and leads to an improved experimental uncertainty of 1.2%. This error changes by at most 20% when the scales, hadronisation factors and PDF parameterisation are changed within the limits defined by their uncertainties. The total error is dominated by the theoretical uncertainty of about 7% mainly due to scale variations.

The determination of the strong coupling from the ratio of the 3-jet to the 2-jet cross section provides an alternative approach to combining the different cross section data. On the one hand the sensitivity of this observable to α_s, which is $\mathcal{O}(\alpha_s)$, is reduced with respect to the 3-jet cross section, which is $\mathcal{O}(\alpha_s^2)$. On the other hand this observable benefits from reduced experimental and theoretical uncertainties (see section 4.2). The common fit of the strong coupling to the 14 ratio points, for which the k-factors are below 2.5 for both the 3-jet and 2-jet cross sections, is given in Table 10. The extracted α_s as a function of μ_r is shown in Fig. 11(b). The experimental uncertainty on α_s increases to 3% with respect to the combined fit from the cross sections. The theoretical uncertainty is reduced to 5% and is dominated by the hadronisation uncertainty.

The strong coupling extracted from all 62 data points (1) agrees well with that obtained from jet cross sections in the higher Q^2 range between 150 and 15000 GeV^2: $\alpha_s(M_Z) = 0.1168 \pm 0.0007(exp.)^{+0.0046}_{-0.0030}(th.) \pm 0.0016(\mathrm{PDF})$ [4]. This agreement is remarkable, given the sensitivity of the NLO prediction to the renormalisation scale in the low Q^2 regime. At high Q^2 [4] the fit was done using the factorisation scale Q, instead of $\sqrt{(Q^2 + P_{T,\,\mathrm{obs}}^2)/2}$ used in this

analysis. However, as was shown in [4], the choice of factorisation scale has only little impact on extracted value of α_s at high Q^2. The value of $\alpha_s(M_Z)$ obtained in this analysis is also consistent with the world averages $\alpha_s(M_Z) = 0.1176 \pm 0.0020$ [37] and $\alpha_s(M_Z) = 0.1184 \pm 0.0007$ [38].

The new low Q^2 measurement together with data from the high Q^2 analysis provides a test of the running of the strong coupling for μ_r between 6 and 70 GeV as illustrated in Fig. 12. A simultaneous fit of α_s from low and high Q^2 data was also performed. It did not lead to an improved precision with respect to the high Q^2 determination alone due to the large theoretical uncertainties at low Q^2.

6 Conclusion

Measurements of the inclusive, 2-jet and 3-jet cross sections in deep-inelastic positron-proton scattering are presented in the range $5 < Q^2 < 100$ GeV^2 and $0.2 < y < 0.7$. Jets are reconstructed using the inclusive k_T algorithm in the Breit frame and are required to have a minimum transverse momentum of 5 GeV. Calculations at NLO QCD, corrected for hadronisation effects, provide a good description of the single and double differential cross sections as functions of the jet transverse momentum P_T, the boson virtuality Q^2 as well as of the proton momentum fraction ξ. The precision of the measurements is typically 6 to 10%.

The strong coupling α_s is determined from a fit of the NLO prediction to the measured jet cross sections. The dominant source of uncertainties is related to the renormalisation scale dependence, which is used to estimate the effect of missing higher orders. The extracted value of the strong coupling

$$\alpha_s(M_Z) = 0.1160 \pm 0.0014(exp.)^{+0.0093}_{-0.0077}(th.) \pm 0.0016(\text{PDF})$$

is consistent with the value determined from high Q^2 jet cross sections. Both measurements test a running of the strong coupling for renormalisation scales μ_r between 6 and 70 GeV.

Acknowledgements

We are grateful to the HERA machine group whose outstanding efforts have made this experiment possible. We thank the engineers and technicians for their work in constructing and maintaining the H1 detector, our funding agencies for financial support, the DESY technical staff for continual assistance and the DESY directorate for support and for the hospitality which they extend to the non–DESY members of the collaboration. We thank Zoltan Nagy for fruitful discussions.

References

[1] R. Feynman, *"Photon–Hadron Interactions"*, Benjamin, New York, 1972.

[2] C. Adloff *et al.* [H1 Collaboration], Eur. Phys. J. C **19** (2001) 289 [hep-ex/0010054].

[3] A. Aktas *et al.* [H1 Collaboration], Phys. Lett. B **653** (2007) 134 [arXiv:0706.3722].

[4] F. D. Aaron *et al.* [H1 Collaboration], Eur. Phys. J. C **65** (2010) 363 [arXiv:0904.3870].

[5] S. Chekanov *et al.* [ZEUS Collaboration], Phys. Lett. B **649** (2007) 12 [hep-ex/0701039].

[6] C. Adloff *et al.* [H1 Collaboration], Phys. Lett. B **542** (2002) 193 [hep-ex/0206029].

[7] S. Chekanov *et al.* [ZEUS Collaboration], Nucl. Phys. B **786** (2007) 152 [arXiv:0705.1931].

[8] I. Abt *et al.* [H1 Collaboration], Nucl. Instrum. Meth. A **386** (1997) 310;
I. Abt *et al.* [H1 Collaboration], Nucl. Instrum. Meth. A **386** (1997) 348.

[9] R.D. Appuhn *et al.* [H1 SPACAL Group], Nucl. Instrum. Meth. A **386** (1997) 397.

[10] D. Pitzl *et al.*, Nucl. Instrum. Meth. A **454** (2000) 334 [hep-ex/0002044].

[11] C. Kleinwort, "H1 Alignment Experience", in Proceedings of the First LHC Detector Alignment Workshop, eds. S. Blusk *et al.*, CERN-2007-004, p.41.

[12] B. Andrieu *et al.* [H1 Calorimeter Group], Nucl. Instrum. Meth. A **336** (1993) 460.

[13] B. Andrieu *et al.* [H1 Calorimeter Group], Nucl. Instrum. Meth. A **336** (1993) 499;
B. Andrieu *et al.* [H1 Calorimeter Group], Nucl. Instrum. Meth. A **350** (1994) 57.

[14] M. Peez, *"Search for deviations from the standard model in high transverse energy processes at the electron proton collider HERA."* (In French), CPPM-T-2003-04 (available at http://www-h1.desy.de/psfiles/theses/).

[15] B. Portheault, *"First measurement of charged and neutral current cross sections with the polarized positron beam at HERA II and QCD-electroweak analyses."* (In French), LAL-05-05 (available at http://www-h1.desy.de/psfiles/theses/).

[16] U. Bassler and G. Bernardi, Nucl. Instrum. Meth. A **361** (1995) 197 [hep-ex/9412004].

[17] S.D. Ellis and D.E. Soper, Phys. Rev. D **48** (1993) 3160 [hep-ph/9305266].

[18] S. Catani *et al.*, Nucl. Phys. B **406** (1993) 187.

[19] S. Frixione and G. Ridolfi, Nucl. Phys. B **507** (1997) 315 [hep-ph/9707345].

[20] K. Charchula, G.A. Schuler and H. Spiesberger, DJANGOH V1.4, Comput. Phys. Commun. **81** (1994) 381.

[21] L. Lonnblad, ARIADNE V4.08, Comput. Phys. Commun. **71** (1992) 15.

[22] H. Jung, RAPGAP V3.1, Comp. Phys. Commun. **86** (1995) 147.

[23] A. Kwiatkowski, H. Spiesberger and H.J. Mohring, HERACLES V4.63, Comp. Phys. Commun. **69** (1992) 155.

[24] B. Andersson *et al.*, Phys. Rep. **97** (1983) 31.

[25] R. Brun *et al.*, GEANT3, CERN-DD/EE/84-1.

[26] B.R. Webber, J. Phys. G **19** (1993) 1567.

[27] Z. Nagy and Z. Trocsanyi, NLOJET++ V4.1.0, Phys. Rev. Lett. **87** (2001) 082001 [hep-ph/0104315].

[28] W. A. Bardeen, A. J. Buras, D. W. Duke and T. Muta, Phys. Rev. D **18** (1978) 3998.

[29] W.K. Tung *et al.*, JHEP **02** (2007) 053 [hep-ph/0611254].

[30] T. Kluge, K. Rabbertz and M. Wobisch, FastNLO 1.0, in Proceedings of the 14th workshop "Deep inelastic scattering DIS2006", eds. M. Kuze, K. Nagano and K. Tokushuku, p. 483 [hep-ph/0609285].

[31] M. Botje, Eur. Phys. J. C **14** (2000) 285 [hep-ph/9912439].

[32] V. Barone, C. Pascaud and F. Zomer, Eur. Phys. J. C **12** (2000) 243 [hep-ph/9907512].

[33] C. Adloff *et al.* [H1 Collaboration], Phys. Lett. B **479** (2000) 358 [hep-ex/0003002].

[34] M. Gouzevitch, *"Measurement of the strong coupling α_s with hadronic jets in deep-inelastic scattering.*" (In French), DESY-THESIS-2008-047 (available at http://www-h1.desy.de/psfiles/theses/).

[35] A.D. Martin *et al.*, Eur. Phys. J. C **63** (2009) 189 [arXiv:0901.0002].

[36] P.M. Nadolsky *et al.*, Phys. Rev. D **D78** (2008) 013004 [arXiv:0802.0007].

[37] C. Amsler *et al.* [Particle Data Group], Phys. Lett. B **667** (2008) 1.

[38] S. Bethke, Eur. Phys. J. C **64** (2009) 689 [arXiv:0908.1135].

NC DIS Selection	$5 < Q^2 < 100\ \mathrm{GeV}^2$, $0.2 < y < 0.7$		
Inclusive jet	$P_T > 5\ \mathrm{GeV}$		$-1.0 < \eta^{\mathrm{jet}}_{\mathrm{Lab}} < 2.5$
2-jet	$P_T^{\mathrm{jet}1},\ P_T^{\mathrm{jet}2} > 5\ \mathrm{GeV}$	$M_{12} > 18\ \mathrm{GeV}$	
3-jet	$P_T^{\mathrm{jet}1},\ P_T^{\mathrm{jet}2},\ P_T^{\mathrm{jet}3} > 5\ \mathrm{GeV}$		

Table 1: The NC DIS and jet selection criteria.

bin number (inclusive and 2-jets)	corresponding Q^2 range
1	$5 < \mathrm{Q}^2 < 7\ \mathrm{GeV}^2$
2	$7 < \mathrm{Q}^2 < 10\ \mathrm{GeV}^2$
3	$10 < \mathrm{Q}^2 < 15\ \mathrm{GeV}^2$
4	$15 < \mathrm{Q}^2 < 20\ \mathrm{GeV}^2$
5	$20 < \mathrm{Q}^2 < 30\ \mathrm{GeV}^2$
6	$30 < \mathrm{Q}^2 < 40\ \mathrm{GeV}^2$
7	$40 < \mathrm{Q}^2 < 100\ \mathrm{GeV}^2$
bin number (3-jets and 3-jets/2-jets)	**corresponding Q^2 range**
I	$5 < \mathrm{Q}^2 < 10\ \mathrm{GeV}^2$
II	$10 < \mathrm{Q}^2 < 20\ \mathrm{GeV}^2$
III	$20 < \mathrm{Q}^2 < 40\ \mathrm{GeV}^2$
IV	$40 < \mathrm{Q}^2 < 100\ \mathrm{GeV}^2$
bin letter	**corresponding P_T or $\langle P_T \rangle$ range**
a	$5 < \mathrm{P_T} < 10\ \mathrm{GeV}$
b	$10 < \mathrm{P_T} < 15\ \mathrm{GeV}$
c	$15 < \mathrm{P_T} < 20\ \mathrm{GeV}$
d	$20 < \mathrm{P_T} < 80\ \mathrm{GeV}$
bin letter	**corresponding ξ range**
A	$0.004 < \xi < 0.006$
B	$0.006 < \xi < 0.010$
C	$0.010 < \xi < 0.025$
D	$0.025 < \xi < 0.050$
E	$0.05 < \xi < 0.1$
F	$0.1 < \xi < 0.3$

Table 2: Nomenclature for the bins in negative four momentum transfer squared Q^2, jet transverse momentum P_T, average transverse momentum of the two leading jets $\langle P_T \rangle$ and momentum fraction ξ used in the following tables.

Inclusive Jet Cross Section $\frac{d\sigma_{jet}}{dQ^2}$

bin	cross section $[pb/GeV^2]$	statistical uncert. [%]	total uncert. [%]	total uncorrelated uncertainty [%]	total correlated uncert. [%]	single contributions to correlated uncertainty: model uncert. [%]	electron energy scale [%]	electron polar angle [%]	hadronic energy scale [%]	hadronisation correction factor	hadronisation correction uncertainty [%]
1	633	0.7	6.7	4.7	4.8	1.7	0.3	0.4	4.2	0.88	5.8
2	421	0.6	7.0	4.9	5.1	2.2	0.2	0.4	4.3	0.89	5.3
3	250	0.6	6.7	4.7	4.9	1.4	0.1	0.7	4.4	0.89	4.7
4	158	0.7	6.6	4.6	4.8	1.4	0.1	0.7	4.3	0.90	4.0
5	96.9	0.7	6.5	4.5	4.7	1.3	0.2	0.5	4.2	0.91	3.5
6	59.7	0.9	6.4	4.4	4.6	1.5	0.1	0.5	4.0	0.91	2.6
7	21.0	0.7	5.9	4.1	4.3	1.3	0.1	0.6	3.7	0.92	1.5

2-Jet Cross Section $\frac{d\sigma_{2-jet}}{dQ^2}$

bin	cross section $[pb/GeV^2]$	statistical uncert. [%]	total uncert. [%]	total uncorrelated uncertainty [%]	total correlated uncert. [%]	single contributions to correlated uncertainty: model uncert. [%]	electron energy scale [%]	electron polar angle [%]	hadronic energy scale [%]	hadronisation correction factor	hadronisation correction uncertainty [%]
1	83.6	1.5	6.8	4.8	4.8	1.2	0.2	0.2	4.4	0.91	2.8
2	56.4	1.4	8.4	5.9	6.0	3.6	0.1	0.5	4.5	0.93	2.9
3	33.9	1.3	7.4	5.2	5.2	1.5	0.1	0.7	4.7	0.93	1.8
4	22.5	1.6	7.7	5.5	5.4	2.0	0.1	0.7	4.8	0.94	1.8
5	14.4	1.4	7.2	5.1	5.1	1.5	0.2	0.5	4.6	0.94	2.0
6	9.70	1.9	7.3	5.2	5.1	1.5	0.1	0.6	4.6	0.94	1.9
7	3.72	1.4	7.2	5.1	5.1	1.2	0.2	0.6	4.7	0.95	1.9

3-Jet Cross Section $\frac{d\sigma_{3-jet}}{dQ^2}$

bin	cross section $[pb/GeV^2]$	statistical uncert. [%]	total uncert. [%]	total uncorrelated uncertainty [%]	total correlated uncert. [%]	single contributions to correlated uncertainty: model uncert. [%]	electron energy scale [%]	electron polar angle [%]	hadronic energy scale [%]	hadronisation correction factor	hadronisation correction uncertainty [%]
I	10.5	2.6	10.8	7.7	7.5	4.6	0.4	0.4	5.6	0.81	6.3
II	4.56	2.7	10.6	7.7	7.4	4.0	0.7	0.8	5.9	0.82	5.5
III	2.05	2.9	10.8	7.9	7.5	4.1	0.7	0.6	6.0	0.80	7.2
IV	0.560	3.8	11.7	8.6	7.9	4.5	1.0	0.6	6.2	0.81	6.1

Table 3: Inclusive jet, 2-jet and 3-jet cross sections in NC DIS measured as a function of Q^2. The measurements refer to the phase-space given in table 1. In the columns 3 to 6 are shown the statistical uncertainty, the total experimental uncertainty, the total uncorrelated uncertainty including the statistical one and the total bin-to-bin correlated uncertainty calculated as the quadratic sum of the following five components: the model dependence, the electron and the hadronic energy scales, the electron polar angle and the luminosity measurement uncertainties. The contributions to correlated uncertainties are listed in columns 7 to 10. The sharing of the uncertainties between correlated and uncorrelated sources is described in detail in section 2.4. The hadronisation correction factors applied to the NLO predictions and their uncertainties are shown in columns 11 and 12. The bin nomenclature of column 1 is defined in table 2.

Inclusive Jet Cross Section $\frac{\mathrm{d}\sigma_{\mathrm{jet}}}{\mathrm{dP_T}}$

bin	cross section [pb/GeV]	statistical uncert. [%]	total uncert. [%]	total uncorrelated uncertainty [%]	total correlated uncert. [%]	single contributions to correlated uncertainty: model uncert. [%]	electron energy scale [%]	electron polar angle [%]	hadronic energy scale [%]	hadronisation correction factor	hadronisation correction uncertainty [%]
a	1250	0.3	6.8	4.7	4.9	2.1	0.2	0.4	4.1	0.89	4.4
b	174	0.7	6.6	4.5	4.7	2.1	0.1	0.5	3.9	0.93	2.8
c	38.3	1.5	9.8	6.9	6.9	3.4	0.3	0.6	5.8	0.95	2.2
d	1.53	2.2	15.3	10.9	10.8	8.1	0.6	0.8	6.9	0.95	1.5

2-Jet Cross Section $\frac{\mathrm{d}\sigma_{2-\mathrm{jet}}}{\mathrm{d}\langle \mathrm{P_T} \rangle}$

bin	cross section [pb/GeV]	statistical uncert. [%]	total uncert. [%]	total uncorrelated uncertainty [%]	total correlated uncert. [%]	single contributions to correlated uncertainty: model uncert. [%]	electron energy scale [%]	electron polar angle [%]	hadronic energy scale [%]	hadronisation correction factor	hadronisation correction uncertainty [%]
a	120	0.8	6.8	4.7	4.9	2.1	0.2	0.4	4.1	0.92	2.1
b	72.5	0.9	7.7	5.4	5.5	2.3	0.1	0.5	4.7	0.94	2.3
c	15.5	2.0	11.1	7.9	7.8	4.9	0.4	0.6	5.9	0.95	2.3
d	0.620	3.0	17.8	12.7	12.5	9.7	0.6	0.8	7.7	0.96	1.8

3-Jet Cross Section $\frac{\mathrm{d}\sigma_{3-\mathrm{jet}}}{\mathrm{d}\langle \mathrm{P_T} \rangle}$

bin	cross section [pb/GeV]	statistical uncert. [%]	total uncert. [%]	total uncorrelated uncertainty [%]	total correlated uncert. [%]	single contributions to correlated uncertainty: model uncert. [%]	electron energy scale [%]	electron polar angle [%]	hadronic energy scale [%]	hadronisation correction factor	hadronisation correction uncertainty [%]
a	11.7	2.5	9.2	6.6	6.3	2.4	0.5	0.5	5.6	0.77	9.5
b	16.1	2.1	9.0	6.4	6.3	2.5	0.6	0.6	5.5	0.81	6.5
c	4.29	3.9	12.7	9.4	8.6	5.3	0.8	0.7	6.6	0.84	3.6
d	0.192	5.6	20.0	14.7	13.6	10.6	1.0	0.9	8.4	0.87	4.1

Table 4: Inclusive jet, 2-jet and 3-jet cross sections in NC DIS measured as a function of P_T for inclusive jet and $\langle P_T \rangle$ of the two leading jets for 2-jet and 3-jet cross sections together with their relative errors and hadronisation correction factors. Other details are given in the caption to table 3. The bin nomenclature is defined in table 2.

Inclusive Jet Cross Section $\frac{\mathrm{d}^2\sigma_{\mathrm{jet}}}{\mathrm{dQ}^2\mathrm{dP}_{\mathrm{T}}}$

bin	cross section $[\mathrm{pb}/\mathrm{GeV}^3]$	statistical uncert. [%]	total uncert. [%]	total uncorrelated uncertainty [%]	total correlated uncert. [%]	single contributions to correlated uncertainty: model uncert. [%]	electron energy scale [%]	electron polar angle [%]	hadronic energy scale [%]	hadronisation correction factor	hadronisation correction uncertainty [%]
1 a	109	0.7	7.1	4.9	5.1	2.1	0.4	0.5	4.3	0.87	6.7
1 b	12.9	1.8	6.1	4.4	4.2	2.7	0.1	0.1	2.9	0.91	3.2
1 c	2.77	3.8	10.1	7.6	6.7	3.4	0.2	0.1	5.6	0.95	3.4
1 d	0.104	6.4	15.0	11.4	9.6	6.6	1.0	1.0	6.7	0.95	3.4
2 a	72.1	0.7	7.6	5.3	5.5	2.9	0.3	0.4	4.4	0.88	6.1
2 b	9.02	1.7	6.6	4.7	4.6	2.9	0.1	0.5	3.3	0.92	2.9
2 c	1.93	3.4	15.8	11.4	11.0	9.4	0.3	0.8	5.4	0.95	3.1
2 d	0.0729	5.8	24.6	17.8	17.0	15.5	0.1	0.6	6.8	0.95	3.1
3 a	42.8	0.6	7.6	5.3	5.4	2.7	0.2	0.6	4.4	0.89	5.2
3 b	5.45	1.6	7.0	5.0	4.9	2.8	0.2	0.7	3.7	0.92	2.9
3 c	1.12	3.3	12.2	8.9	8.4	6.0	0.2	0.8	5.6	0.95	2.8
3 d	0.0484	5.5	20.5	15.0	14.0	12.0	0.7	1.0	7.0	0.95	2.8
4 a	26.7	0.8	7.3	5.1	5.2	2.7	0.1	0.6	4.2	0.90	4.3
4 b	3.68	1.9	7.6	5.4	5.3	2.7	0.1	0.7	4.2	0.93	2.7
4 c	0.783	3.9	12.6	9.2	8.5	6.1	0.4	0.8	5.7	0.94	4.1
4 d	0.0326	6.5	17.2	13.0	11.3	8.9	0.5	0.8	6.8	0.95	4.1
5 a	16.4	0.7	7.0	4.8	5.0	2.5	0.3	0.5	4.1	0.90	3.7
5 b	2.21	1.8	7.5	5.4	5.3	2.5	0.1	0.4	4.4	0.94	3.0
5 c	0.508	3.5	10.2	7.6	6.9	2.8	0.3	0.6	6.1	0.95	3.0
5 d	0.0198	5.6	15.0	11.2	9.9	7.1	0.4	0.6	6.7	0.96	2.9
6 a	9.72	1.0	7.3	5.1	5.2	3.2	0.1	0.6	3.8	0.91	2.6
6 b	1.65	2.2	8.6	6.2	5.9	3.3	0.2	0.5	4.6	0.95	2.6
6 c	0.383	4.5	11.1	8.4	7.3	3.7	0.2	0.5	6.1	0.96	5.2
6 d	0.0120	7.5	15.0	11.8	9.3	5.4	0.7	0.6	7.3	0.94	2.8
7 a	3.37	0.8	6.5	4.5	4.7	2.8	0.1	0.7	3.4	0.91	1.5
7 b	0.614	1.7	9.5	6.7	6.7	4.2	0.2	0.6	5.0	0.96	1.7
7 c	0.146	3.3	10.6	7.8	7.2	2.8	0.4	0.6	6.4	0.94	2.7
7 d	0.00677	5.3	12.0	9.2	7.7	2.5	0.6	0.6	7.1	0.96	2.6

Table 5: Double differential inclusive jet cross sections as a function of Q^2 and P_T together with their relative errors and hadronisation correction factors. Other details are given in the caption to table 3. The bin nomenclature is defined in table 2.

2-Jet Cross Section $\frac{\mathrm{d}^2\sigma_{2-\mathrm{jet}}}{\mathrm{dQ}^2\mathrm{d}\langle \mathrm{P_T}\rangle}$

bin	cross section $[\mathrm{pb}/\mathrm{GeV}^3]$	statistical uncert. [%]	total uncert. [%]	total uncorrelated uncertainty [%]	total correlated uncert. [%]	single contributions to correlated uncertainty: model uncert. [%]	electron energy scale [%]	electron polar angle [%]	hadronic energy scale [%]	hadronisation correction factor	hadronisation correction uncertainty [%]
1 a	10.1	2.0	6.7	4.8	4.6	1.9	0.6	0.5	3.9	0.91	3.3
1 b	5.06	2.6	7.6	5.6	5.1	2.2	0.1	0.2	4.4	0.91	2.8
1 c	1.08	5.5	11.5	8.9	7.2	4.6	0.4	0.2	5.4	0.95	2.8
1 d	0.0435	8.3	16.7	13.1	10.3	6.3	1.0	0.9	7.9	0.96	2.7
2 a	6.55	1.8	6.7	4.8	4.7	1.7	0.3	0.3	4.1	0.91	3.4
2 b	3.56	2.4	8.2	6.0	5.7	3.1	0.1	0.6	4.5	0.93	3.0
2 c	0.767	5.0	18.8	13.7	12.9	11.4	0.2	0.8	5.6	0.95	2.4
2 d	0.0289	7.8	27.5	20.2	18.7	17.1	0.2	0.8	7.3	0.94	3.0
3 a	3.78	1.8	7.4	5.2	5.1	2.1	0.2	0.7	4.4	0.92	1.7
3 b	2.28	2.2	7.9	5.7	5.4	2.3	0.2	0.7	4.6	0.94	2.8
3 c	0.441	4.9	15.1	11.2	10.2	7.9	0.3	0.7	6.1	0.94	2.8
3 d	0.0201	7.3	22.7	16.8	15.2	13.1	0.7	1.0	7.5	0.96	3.0
4 a	2.45	2.3	7.3	5.3	5.0	1.8	0.2	0.7	4.4	0.94	1.5
4 b	1.52	2.7	8.1	5.9	5.5	2.0	0.1	0.8	4.8	0.94	2.2
4 c	0.327	5.7	13.5	10.3	8.8	6.3	0.4	0.9	5.8	0.92	1.8
4 d	0.0135	8.7	20.6	15.8	13.3	10.8	0.6	0.8	7.5	0.97	3.0
5 a	1.64	2.0	6.8	4.9	4.7	1.8	0.4	0.4	4.1	0.93	2.0
5 b	0.927	2.5	8.1	5.9	5.6	2.2	0.1	0.5	4.9	0.95	2.2
5 c	0.213	5.1	10.5	8.2	6.6	2.5	0.3	0.6	5.8	0.96	2.2
5 d	0.00763	7.8	20.1	15.2	13.1	10.3	0.5	0.6	8.0	0.96	2.8
6 a	0.968	2.7	7.2	5.3	4.8	2.3	0.1	0.6	4.0	0.93	1.8
6 b	0.753	3.1	8.8	6.5	5.9	2.6	0.2	0.5	5.0	0.95	1.9
6 c	0.138	6.3	11.5	9.2	6.9	2.8	0.4	0.5	6.0	0.95	4.5
6 d	0.00521	9.9	18.1	14.5	10.8	7.0	0.7	0.7	8.0	0.97	4.4
7 a	0.379	2.1	6.7	4.9	4.7	1.7	0.1	0.6	4.0	0.94	1.8
7 b	0.266	2.4	8.2	5.9	5.6	1.8	0.4	0.6	5.1	0.96	1.8
7 c	0.0648	4.8	11.2	8.6	7.3	1.8	0.6	0.6	6.8	0.96	2.7
7 d	0.00265	7.0	15.7	12.1	10.0	5.9	0.5	0.5	7.9	0.95	1.8

Table 6: Double differential 2-jet cross sections as a function of Q^2 and $\langle P_T \rangle$ of two leading jets together with their relative errors and hadronisation correction factors. Other details are given in the caption to table 3. The bin nomenclature is defined in table 2.

2-Jet Cross Section $\frac{\mathrm{d}^2\sigma_{2-\mathrm{jet}}}{\mathrm{d}Q^2\mathrm{d}\xi}$

bin	cross section $[\mathrm{pb}/\mathrm{GeV}^2]$	statistical uncert. [%]	total uncert. [%]	total uncorrelated uncertainty [%]	total correlated uncert. [%]	single contributions to correlated uncertainty: model uncert. [%]	electron energy scale [%]	electron polar angle [%]	hadronic energy scale [%]	hadronisation correction factor	hadronisation correction uncertainty [%]
1 A	608	9.7	35.3	25.9	24.1	23.6	1.2	0.6	4.3	0.94	10.2
1 B	3450	3.4	10.0	7.4	6.7	5.5	0.5	0.3	3.5	0.96	7.0
1 C	3060	2.1	7.2	5.2	5.0	2.8	0.8	1.0	3.6	0.92	3.3
1 D	687	3.4	8.4	6.4	5.4	2.7	0.4	1.4	4.2	0.87	3.3
1 E	76.6	7.2	15.1	11.8	9.4	7.4	0.6	1.1	5.4	0.85	3.4
1 F	4.40	15.8	35.0	27.2	22.1	20.7	1.3	0.9	7.2	0.92	3.1
2 A	723	9.7	12.4	11.1	5.6	4.4	1.8	0.8	2.3	0.97	7.6
2 B	2470	3.3	6.9	5.3	4.4	2.2	0.7	0.6	3.4	0.97	7.0
2 C	2060	1.8	6.8	4.9	4.7	2.2	0.3	0.4	3.9	0.93	3.6
2 D	441	3.0	10.0	7.3	6.8	5.1	0.3	0.5	4.2	0.89	1.7
2 E	50.7	6.3	19.4	14.4	13.0	11.5	0.9	0.5	5.8	0.87	1.7
2 F	2.31	15.2	42.2	31.7	27.9	26.9	1.7	0.4	7.2	0.87	2.0
3 A	363	10.4	13.6	12.1	6.3	1.5	0.6	1.0	5.8	1.02	5.2
3 B	1430	3.3	6.9	5.3	4.4	1.6	0.9	0.7	3.7	0.97	4.5
3 C	1250	1.8	6.7	4.8	4.7	1.7	0.2	0.7	4.1	0.93	1.9
3 D	261	3.0	7.4	5.5	4.9	1.2	0.2	0.7	4.4	0.90	2.1
3 E	38.2	5.6	18.6	13.7	12.6	10.8	1.4	0.9	6.1	0.88	2.1
3 F	1.21	16.0	38.0	29.2	24.3	23.0	2.3	1.2	7.2	0.87	4.0
4 A	231	13.9	15.0	14.4	4.2	1.8	0.8	0.6	3.4	1.09	3.0
4 B	1020	4.0	7.9	6.2	5.0	1.6	1.0	0.6	4.3	0.97	5.1
4 C	782	2.2	6.7	4.9	4.6	1.0	0.3	0.7	4.1	0.95	1.9
4 D	189	3.5	7.7	5.9	5.0	1.1	0.3	0.8	4.5	0.90	2.0
4 E	26.3	6.7	17.2	13.0	11.2	9.2	1.3	0.8	6.0	0.87	1.5
4 F	0.946	17.4	26.7	22.5	14.3	13.0	1.5	0.7	5.5	0.90	1.4
5 A	82	14.3	15.4	14.8	4.3	2.2	0.6	0.5	3.3	1.04	4.3
5 B	602	3.7	7.0	5.5	4.3	2.1	1.1	0.4	3.2	0.98	3.8
5 C	523	1.9	6.8	4.9	4.7	1.6	0.4	0.5	4.1	0.95	2.4
5 D	120	3.1	7.9	5.9	5.2	1.7	0.4	0.6	4.6	0.90	1.0
5 E	16.6	5.9	11.2	8.9	6.9	2.9	1.0	0.6	5.9	0.87	1.1
5 F	0.700	14.3	29.5	23.1	18.3	16.4	1.9	0.9	7.7	0.91	1.7
6 A	33.9	20.9	21.6	21.2	4.3	2.1	1.7	0.2	2.9	0.98	6.8
6 B	431	5.0	7.3	6.2	3.9	0.9	0.7	0.6	3.4	0.99	2.3
6 C	335	2.5	7.1	5.3	4.8	2.2	0.4	0.5	4.0	0.95	2.9
6 D	93.8	4.0	8.7	6.7	5.6	2.2	0.3	0.5	4.8	0.91	0.9
6 E	9.52	7.9	12.6	10.5	7.1	3.0	1.5	0.7	6.0	0.89	1.0
6 F	0.427	18.9	27.7	23.7	14.4	12.3	1.8	0.5	6.9	0.91	2.2
7 A	4.83	44.7	45.5	45.1	6.3	4.8	0.8	0.8	3.5	1.17	5.2
7 B	122	5.2	9.6	7.7	5.7	3.7	0.9	0.3	4.0	0.98	1.9
7 C	131	2.0	7.2	5.1	5.0	2.9	0.1	0.4	3.8	0.96	1.4
7 D	36.5	2.7	8.8	6.5	5.9	3.1	0.6	0.5	4.8	0.94	1.4
7 E	5.81	4.9	11.6	8.9	7.5	3.1	1.5	0.4	6.4	0.90	1.5
7 F	0.237	11.8	22.1	17.7	13.2	10.3	2.3	0.4	7.8	0.89	2.7

Table 7: Double differential 2-jet cross sections as a function of Q^2 and ξ together with their relative errors and hadronisation correction factors. Other details are given in the caption to table 3. The bin nomenclature is defined in table 2.

3-Jet Cross Section $\frac{\mathrm{d}^2\sigma_{3-\mathrm{jet}}}{\mathrm{dQ}^2\mathrm{d}\langle\mathrm{P_T}\rangle}$

bin	cross section $[\mathrm{pb}/\mathrm{GeV}^3]$	statistical uncert. [%]	total uncert. [%]	total uncorrelated uncertainty [%]	total correlated uncert. [%]	single contributions to correlated uncertainty: model uncert. [%]	electron energy scale [%]	electron polar angle [%]	hadronic energy scale [%]	hadronisation correction factor	hadronisation correction uncertainty [%]
I a	0.780	4.3	10.0	7.6	6.5	3.2	0.3	0.2	5.4	0.78	11.4
I b	0.951	3.8	9.6	7.2	6.4	3.4	0.3	0.4	5.1	0.81	6.0
I c	0.240	7.2	20.4	15.2	13.5	11.8	0.7	0.6	6.3	0.82	5.8
I d	0.0102	10.9	24.3	18.8	15.4	12.6	0.8	1.1	8.5	0.88	5.5
II a	0.321	4.5	10.5	8.0	6.8	2.9	0.6	0.9	5.8	0.78	8.4
II b	0.409	3.9	10.0	7.5	6.6	3.1	0.6	0.8	5.5	0.82	6.4
II c	0.113	7.3	17.3	13.3	11.2	8.9	0.8	0.9	6.5	0.84	4.8
II d	0.00526	10.3	24.4	18.7	15.7	13.1	1.1	0.9	8.4	0.87	4.7
III a	0.126	5.0	10.8	8.3	6.8	3.7	0.5	0.7	5.5	0.76	10.3
III b	0.203	4.2	10.9	8.2	7.2	3.9	0.7	0.6	5.8	0.81	6.6
III c	0.0503	7.6	13.9	11.1	8.3	4.0	0.8	0.5	7.0	0.86	6.4
III d	0.00231	10.6	22.4	17.5	14.0	11.0	1.1	0.7	8.3	0.87	4.4
IV a	0.0350	6.8	13.1	10.4	8.0	5.0	0.7	0.5	5.9	0.78	7.1
IV b	0.0513	5.5	13.9	10.5	9.1	6.6	1.2	0.7	5.9	0.82	7.1
IV c	0.0167	9.7	14.9	12.5	8.1	3.0	1.3	0.8	7.2	0.85	5.3
IV d	0.000750	14.1	20.6	17.6	10.6	7.0	1.4	0.7	7.7	0.85	5.3

Table 8: Double differential 3-jet cross sections as a function of Q^2 and $\langle P_T \rangle$ of two leading jets together with their relative errors and hadronisation correction factors. Other details are given in the caption to table 3. The bin nomenclature is defined in table 2.

3-Jet to 2-Jet Cross Sections Ratio $\frac{\mathrm{d}\sigma_{3-\mathrm{jet}}}{\mathrm{dQ}^2} \Big/ \frac{\mathrm{d}\sigma_{2-\mathrm{jet}}}{\mathrm{dQ}^2}$

bin	3-jet/2-jet ratio	statistical uncert. [%]	total uncert. [%]	total uncorrelated uncertainty [%]	total correlated uncert. [%]	single contributions to correlated uncertainty: model uncert. [%]	electron energy scale [%]	electron polar angle [%]	hadronic energy scale [%]	hadronisation correction factor	hadronisation correction uncertainty [%]
I	0.156	2.4	6.8	5.0	4.6	4.2	0.6	0.3	1.2	0.88	4.7
II	0.162	2.5	6.1	4.6	4.1	3.6	0.7	0.1	1.2	0.88	5.1
III	0.170	2.4	5.1	3.8	3.4	2.6	0.8	0.1	1.4	0.85	6.9
IV	0.151	3.7	8.0	6.2	5.1	4.6	0.8	0.1	1.5	0.85	6.8

3-Jet to 2-Jet Cross Sections Ratio $\frac{\mathrm{d}\sigma_{3-\mathrm{jet}}}{\mathrm{d}\langle \mathrm{P_T} \rangle} \Big/ \frac{\mathrm{d}\sigma_{2-\mathrm{jet}}}{\mathrm{d}\langle \mathrm{P_T} \rangle}$

bin	3-jet/2-jet ratio	statistical uncert. [%]	total uncert. [%]	total uncorrelated uncertainty [%]	total correlated uncert. [%]	single contributions to correlated uncertainty: model uncert. [%]	electron energy scale [%]	electron polar angle [%]	hadronic energy scale [%]	hadronisation correction factor	hadronisation correction uncertainty [%]
a	0.0982	2.4	4.1	3.1	2.6	1.2	0.7	0.1	1.5	0.84	8.5
b	0.222	1.9	3.2	2.4	2.1	1.2	0.4	0.1	0.7	0.86	5.2
c	0.276	3.5	4.8	4.1	2.5	1.9	0.4	0.1	0.7	0.89	3.0
d	0.310	5.1	6.8	5.9	3.3	2.9	0.4	0.1	0.7	0.91	2.9

3-Jet to 2-Jet Cross Sections Ratio $\frac{\mathrm{d}^2\sigma_{3-\mathrm{jet}}}{\mathrm{dQ}^2\mathrm{d}\langle \mathrm{P_T} \rangle} \Big/ \frac{\mathrm{d}^2\sigma_{2-\mathrm{jet}}}{\mathrm{dQ}^2\mathrm{d}\langle \mathrm{P_T} \rangle}$

bin	3-jet/2-jet ratio	statistical uncert. [%]	total uncert. [%]	total uncorrelated uncertainty [%]	total correlated uncert. [%]	single contributions to correlated uncertainty: model uncert. [%]	electron energy scale [%]	electron polar angle [%]	hadronic energy scale [%]	hadronisation correction factor	hadronisation correction uncertainty [%]
I a	0.0980	4.1	6.7	5.5	3.9	3.2	0.7	0.2	1.4	0.85	10.2
I b	0.228	3.5	6.6	5.2	4.1	3.7	0.3	0.2	0.7	0.87	5.0
I c	0.267	6.3	12.0	9.5	7.4	7.2	0.3	0.1	0.8	0.87	5.1
I d	0.294	10.2	12.4	11.3	5.2	4.8	0.2	0.3	0.9	0.93	5.3
II a	0.103	4.4	6.6	5.5	3.6	2.8	0.8	0.2	1.4	0.84	9.2
II b	0.215	3.7	5.7	4.7	3.3	2.8	0.4	0.1	0.8	0.88	6.0
II c	0.293	6.9	9.7	8.4	5.0	4.7	0.4	0.1	0.5	0.90	4.3
II d	0.312	9.2	12.0	10.7	5.5	5.2	0.5	0.2	0.9	0.91	7.6
III a	0.0966	4.6	7.2	6.0	4.1	3.4	0.9	0.2	1.4	0.81	11.0
III b	0.243	3.2	4.9	4.0	2.8	2.2	0.6	0.1	0.9	0.85	6.9
III c	0.287	6.9	9.8	8.4	5.1	4.7	0.4	0.1	1.1	0.90	8.4
III d	0.359	9.4	14.0	11.9	7.4	7.2	0.5	0.1	0.4	0.90	8.5
IV a	0.0922	6.7	10.9	9.0	6.2	5.6	0.6	0.2	2.0	0.83	8.8
IV b	0.193	5.5	11.0	8.6	6.8	6.5	0.8	0.1	0.8	0.85	8.8
IV c	0.257	9.0	13.3	11.3	6.9	6.7	0.7	0.2	0.4	0.89	6.6
IV d	0.282	14.1	16.1	15.1	5.6	5.3	0.9	0.2	0.2	0.90	6.3

Table 9: Ratio of 3-jet to 2-jet cross sections as a function of Q^2 and $\langle P_T \rangle$ together with their relative errors and hadronisation correction factors. Other details are given in the caption to table 3. The bin nomenclature is defined in table 2.

Determination of α_s from jets

Measurement	$\alpha_S(M_Z)$	Uncertainty			χ^2/ndf
		experimental	theory	PDF	
$\sigma_{\mathrm{jet}}\,(Q^2, P_T)$	0.1180	0.0018	$^{+0.0122}_{-0.0090}$	0.0022	$17.5/21$
$\sigma_{\text{2-jet}}\,(Q^2, \langle P_T \rangle)$	0.1155	0.0018	$^{+0.0121}_{-0.0090}$	0.0025	$14.3/23$
$\sigma_{\text{3-jet}}\,(Q^2, \langle P_T \rangle)$	0.1170	0.0017	$^{+0.0090}_{-0.0072}$	0.0014	$11.0/15$
$\sigma_{\mathrm{jet}},\ \sigma_{\text{2-jet}},\ \sigma_{\text{3-jet}}$	0.1160	0.0014	$^{+0.0093}_{-0.0077}$	0.0016	$50.6/61$
$\sigma_{\text{3-jet}}/\sigma_{\text{2-jet}}$	0.1215	0.0032	$^{+0.0066}_{-0.0058}$	0.0013	$11.9/13$

Table 10: Values of $\alpha_s(M_Z)$ obtained from fits to the individual inclusive jet, 2-jet and 3-jet double differential cross sections and from a simultaneous fit to all of them and to the ratio of 3-jet to 2-jet cross sections. Fitted values are given with experimental, theoretical and PDF errors, the normalised χ^2/ndf of the fit is also shown.

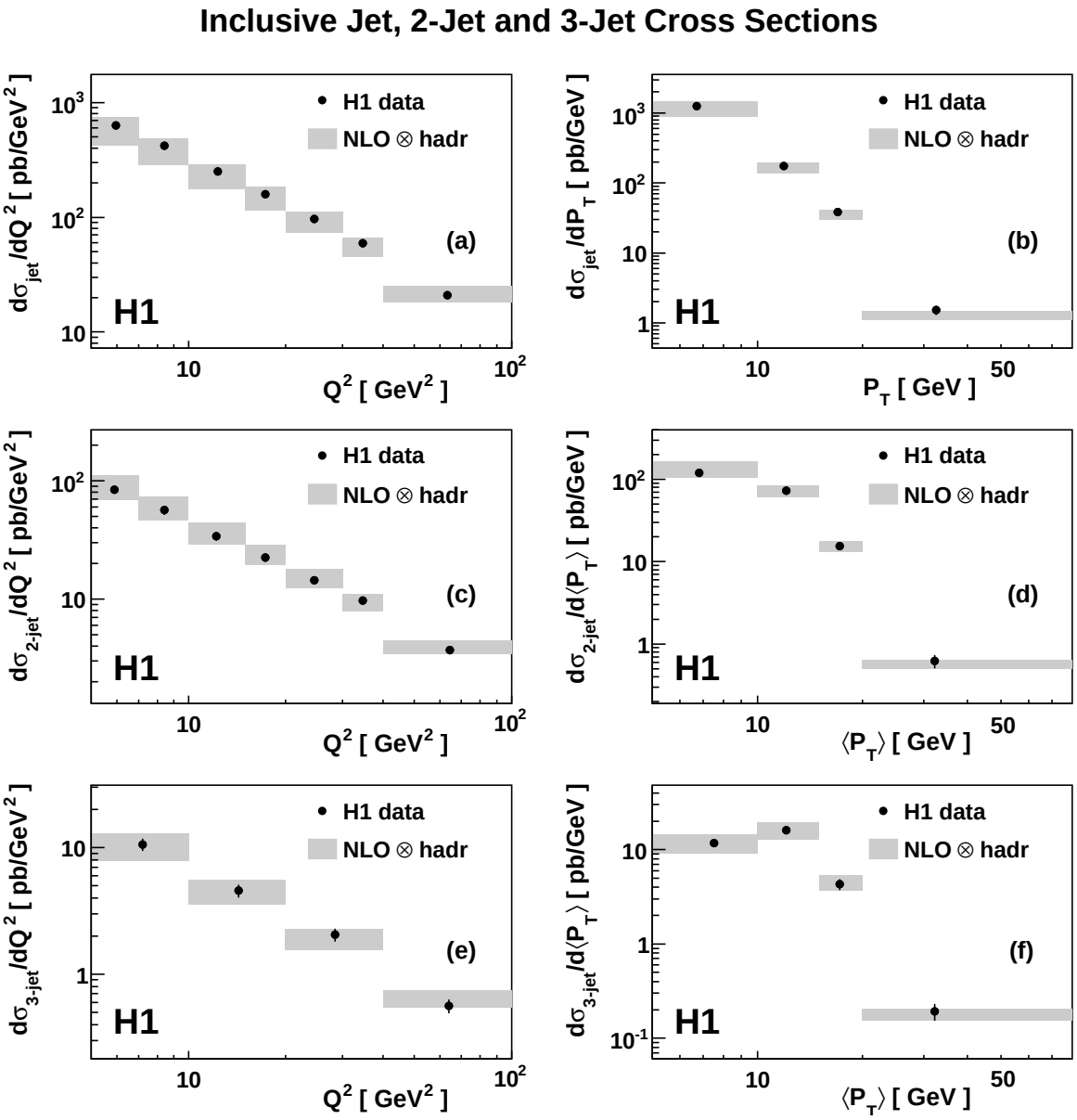

Figure 2: Inclusive jet cross sections $d\sigma_{jet}/dQ^2$ (a) and $d\sigma_{jet}/dP_T$ (b), 2-jet cross sections $d\sigma_{2-jet}/dQ^2$ (c) and $d\sigma_{2-jet}/d\langle P_T\rangle$ (d) and 3-jet cross sections $d\sigma_{3-jet}/dQ^2$ (e) and $d\sigma_{3-jet}/d\langle P_T\rangle$ (f), compared with NLO QCD predictions corrected for hadronisation. The error bars show the total experimental uncertainty, defined as the quadratic sum of the statistical and systematic uncertainties. The points are shown at the average values of Q^2, P_T or $\langle P_T\rangle$ within each bin. The NLO QCD predictions are shown together with the theory uncertainties associated with the scale uncertainties and the hadronisation (grey band).

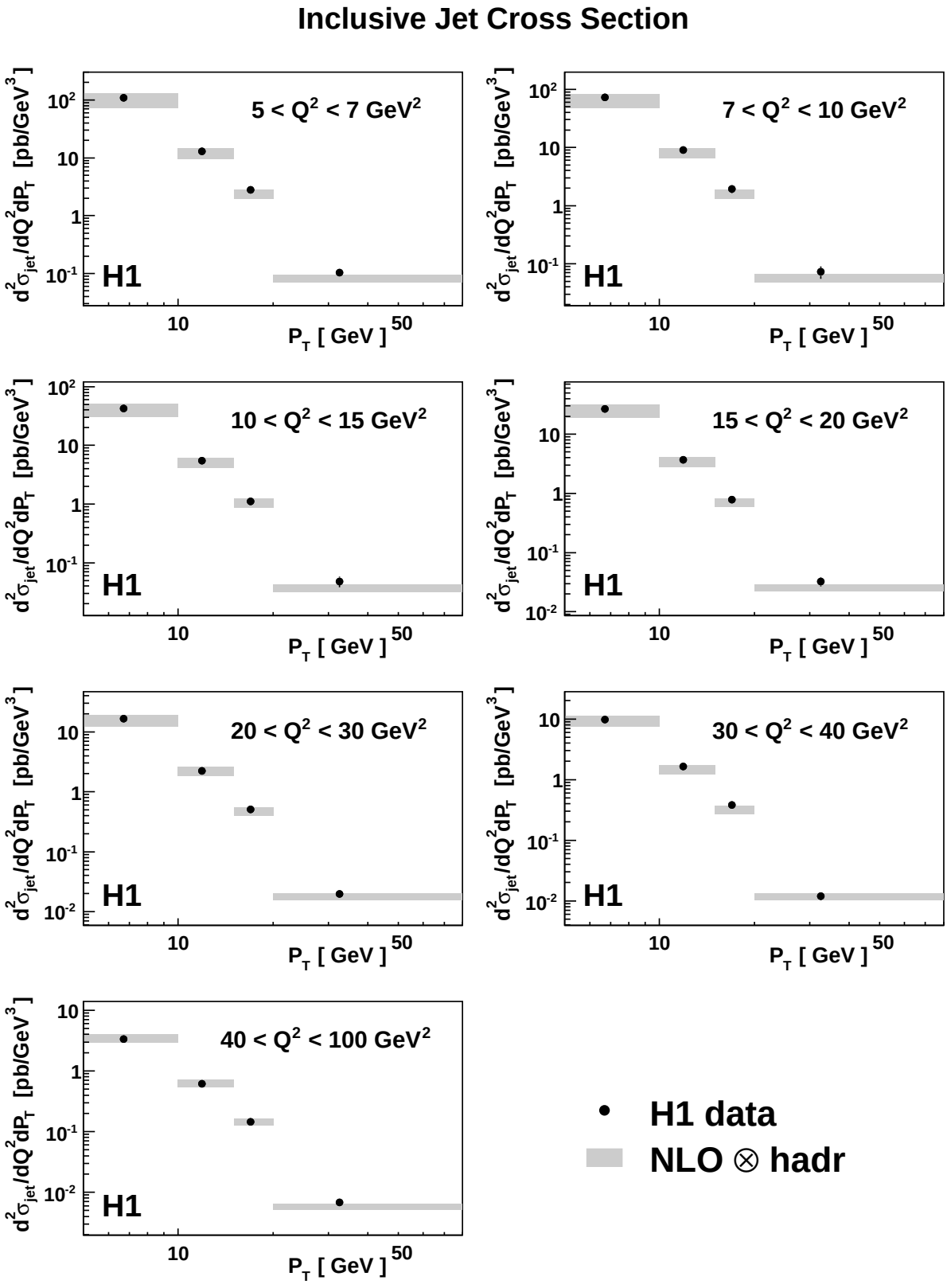

Figure 3: Double differential inclusive jet cross sections as a function of Q^2 and P_T, compared with NLO QCD predictions corrected for hadronisation. Other details are given in the caption to Fig. 2.

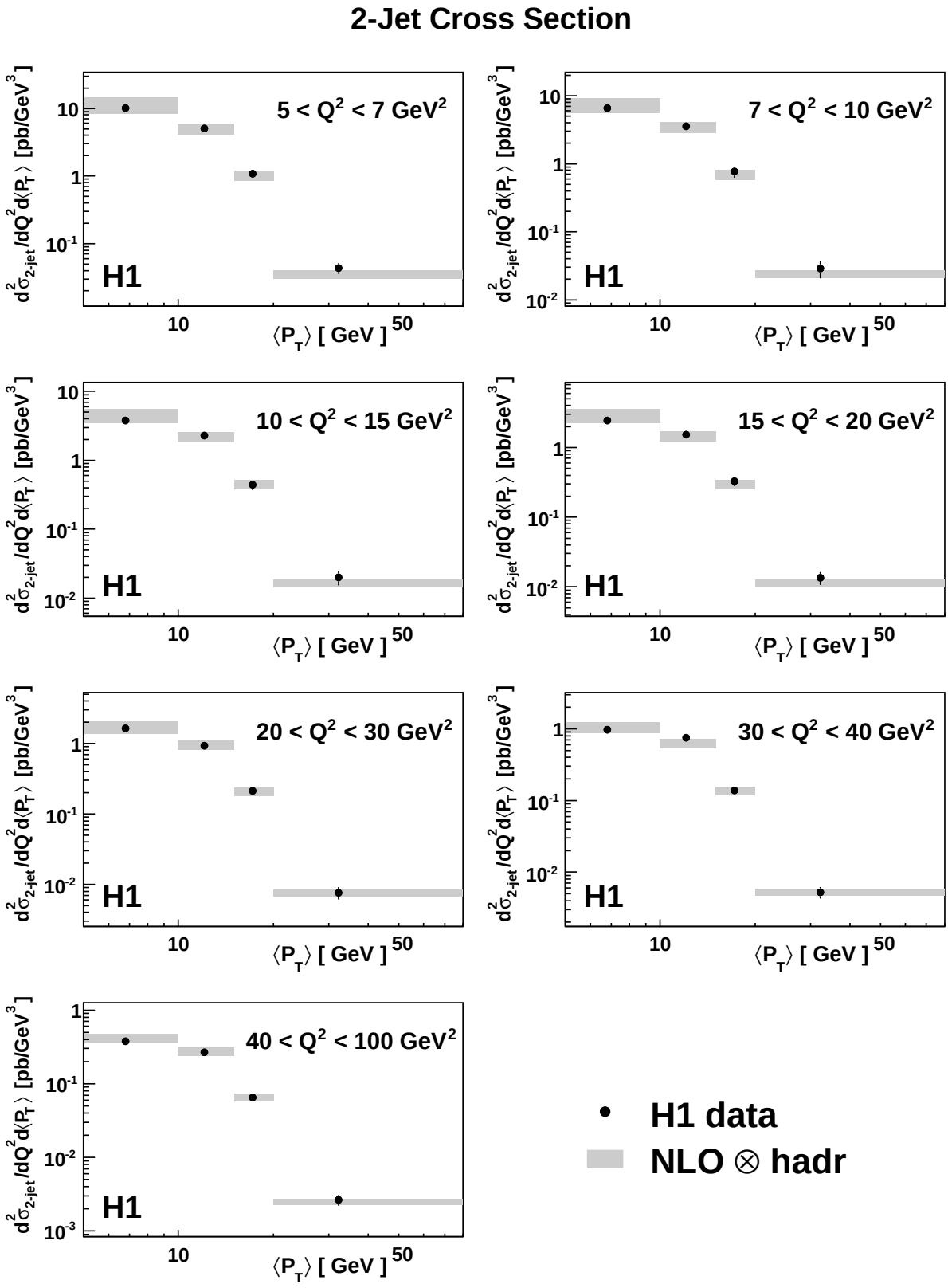

Figure 4: Double differential 2-jet cross sections as a function of Q^2 and $\langle P_T \rangle$, compared with NLO QCD predictions corrected for hadronisation. Other details are given in the caption to Fig. 2.

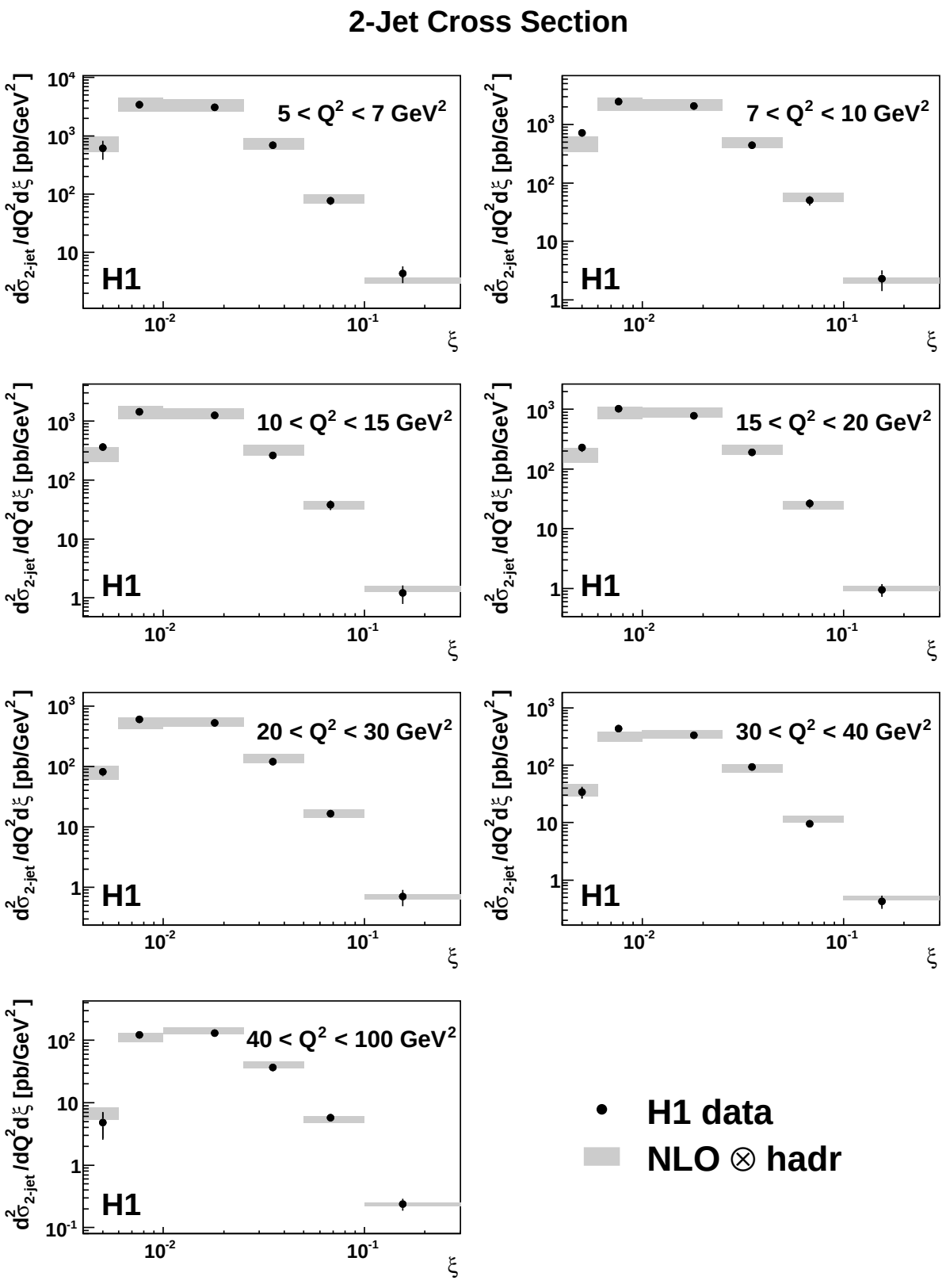

Figure 5: Double differential 2-jet cross section, as a function of Q^2 and ξ, compared with NLO QCD predictions corrected for hadronisation. Other details are given in the caption to Fig. 2.

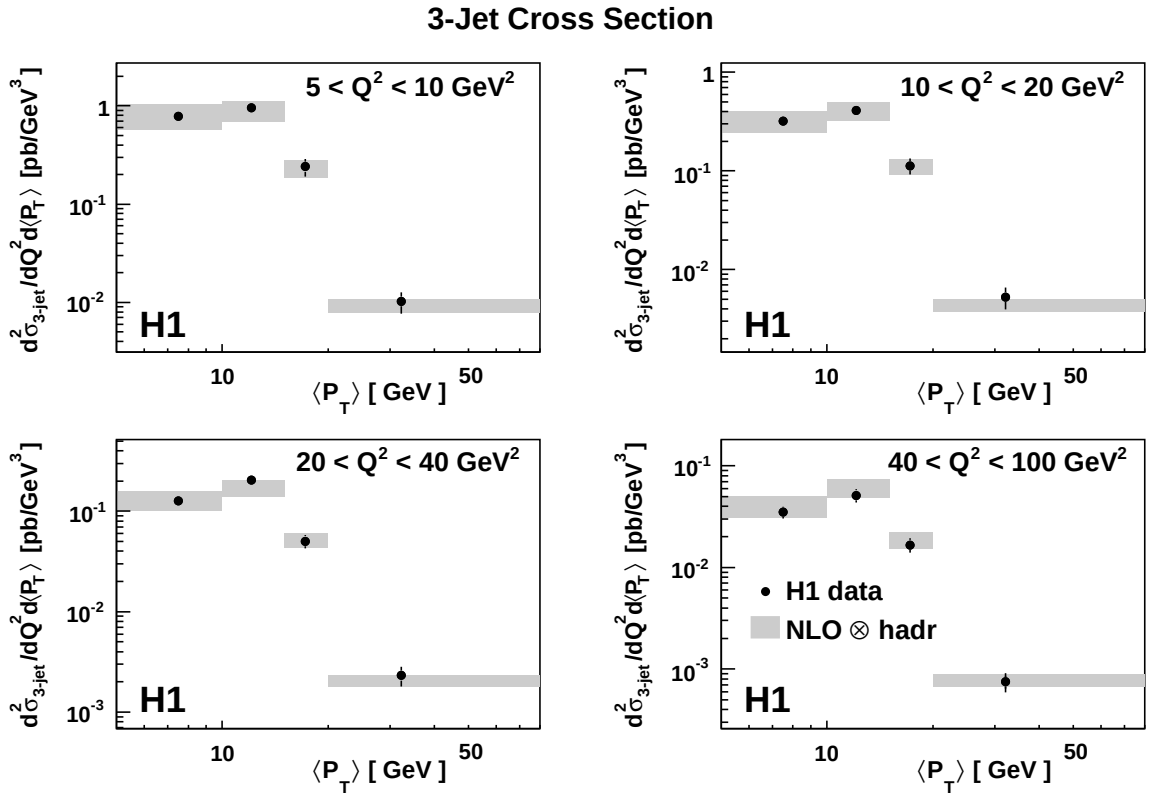

Figure 6: Double differential 3-jet cross sections as a function of Q^2 and $\langle P_T \rangle$, compared with NLO QCD predictions corrected for hadronisation. Other details are given in the caption to Fig. 2.

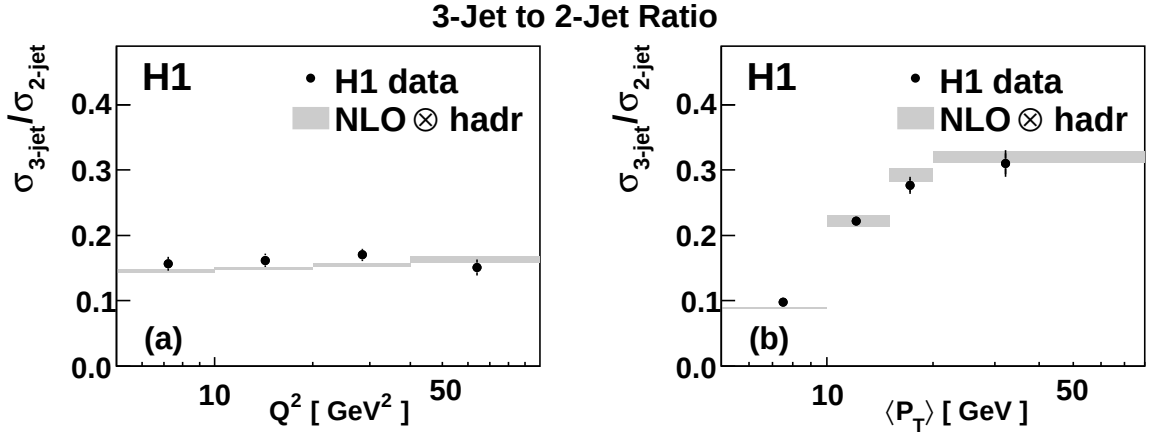

Figure 7: Ratios of 3-jet to 2-jet cross sections as a function of Q^2 (a) and $\langle P_T \rangle$ integrated over the full Q^2 range (b) compared with NLO QCD predictions corrected for hadronisation. Other details are given in the caption to Fig. 2.

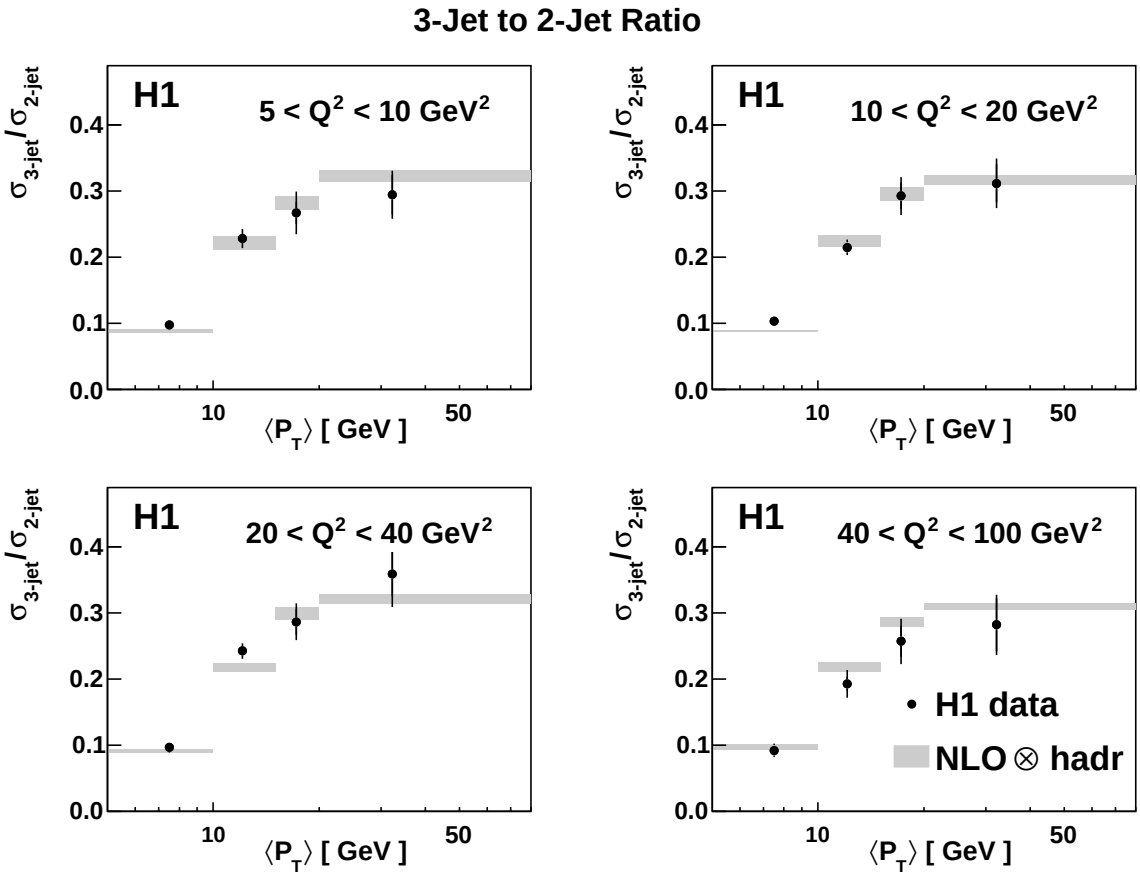

Figure 8: Ratios of 3-jet to 2-jet cross sections as a function of $\langle P_T \rangle$ in four different Q^2 ranges compared with NLO QCD predictions corrected for hadronisation. Other details are given in the caption to Fig. 2.

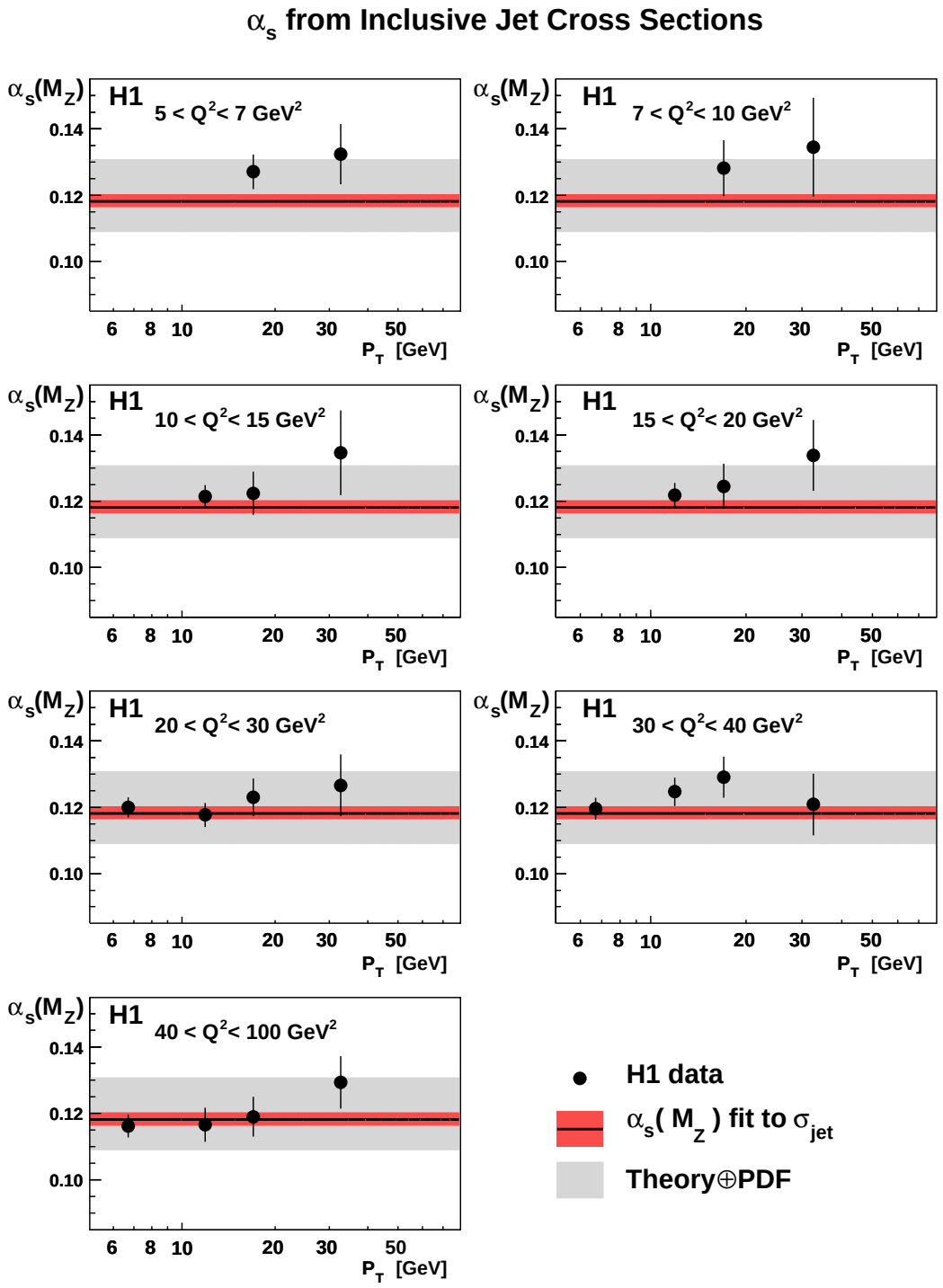

Figure 9: Values of $\alpha_s(M_Z)$ determined using the inclusive jet cross sections measured in 22 bins in Q^2 and P_T with the k-factor below 2.5. The error bars denote the total experimental uncertainty of each data point. The solid line shows the two loop solution of the renormalisation group equation, $\alpha_s(M_Z)$, obtained from a simultaneous fit of all 22 measurements of the inclusive jet cross sections. The inner band denotes the experimental uncertainty and the outer band denotes the squared sum of the PDF uncertainty and the theoretical uncertainties associated with the renormalisation and factorisation scales and the model dependence of the hadronisation corrections.

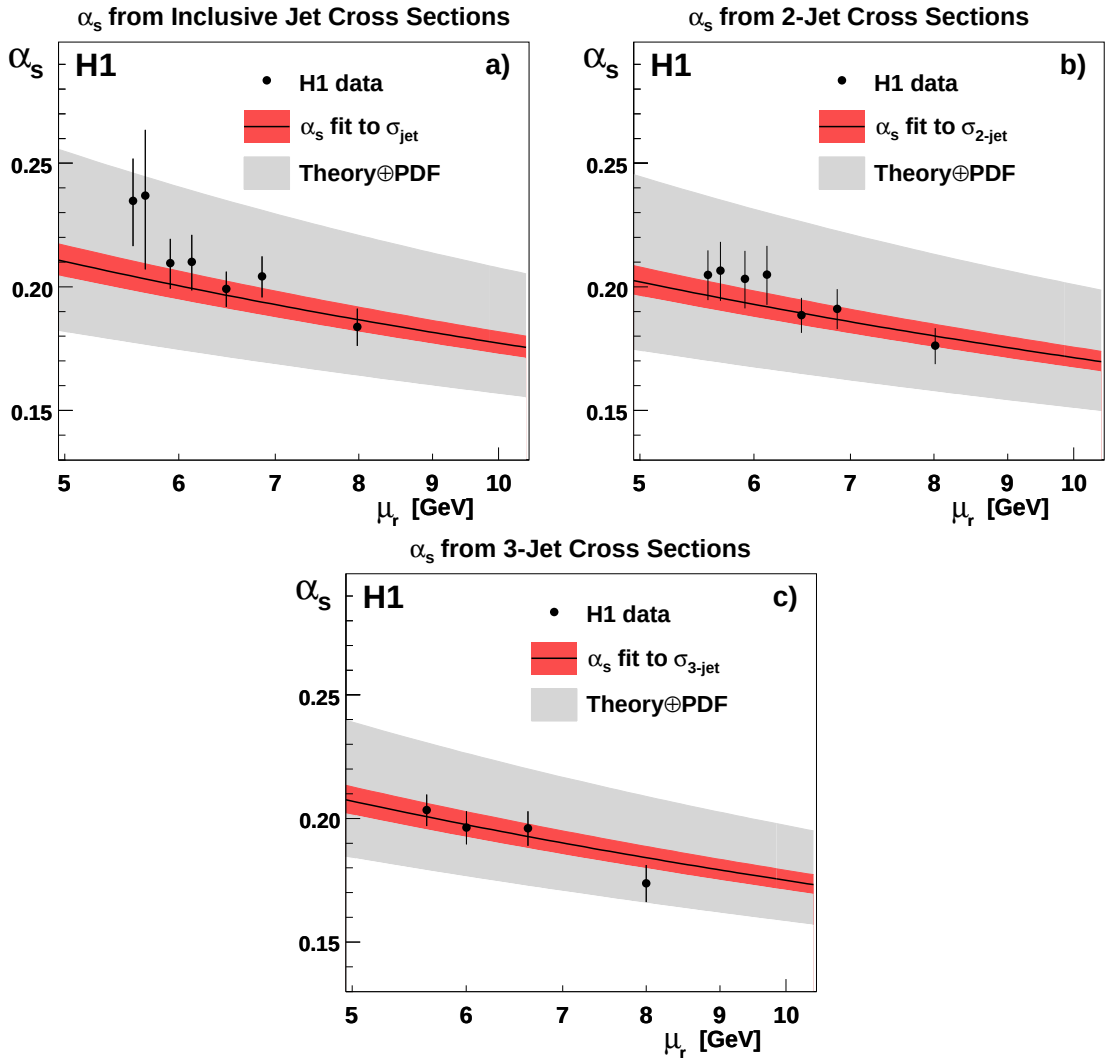

Figure 10: Values of $\alpha_s(\mu_r = \sqrt{(Q^2 + P^2_{T,\,\mathrm{obs}})/2})$ extracted from inclusive jet cross section (a), 2-jet cross section (b) and 3-jet cross section (c). In each case, the solid lines show the two loop solution of the renormalisation group equation obtained by evolving the corresponding fitted value of $\alpha_s(M_Z)$, as summarized in table 10, data rows 1-3. Other details are given in the caption to Fig. 9.

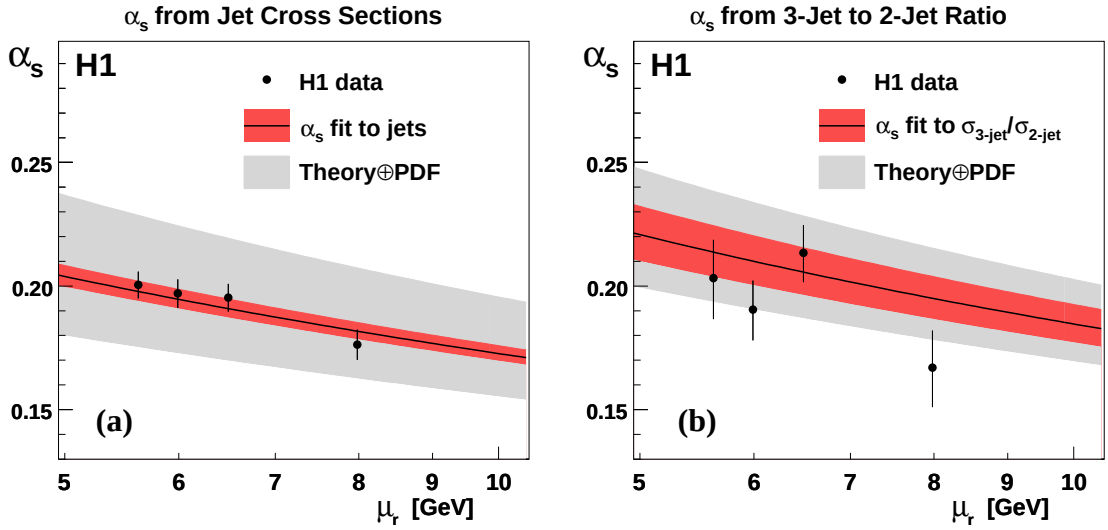

Figure 11: Values of $\alpha_s(\mu_r = \sqrt{(Q^2 + P^2_{T,\,\mathrm{obs}})/2})$ obtained by a simultaneous fit of all jet cross sections in each Q^2 bin (a) and of the ratio of 3-jet cross section to 2-jet cross section (b). The solid lines show the two loop solution of the renormalisation group equation obtained by evolving the α_s obtained from these measurements. For (a) the value of α_s is extracted from a simultaneous fit of 62 measurements of inclusive jet, 2-jet and 3-jet double differential cross sections in bins of Q^2 and P_T ($\langle P_T \rangle$ for 2-jets and 3-jets) with k-factor below 2.5, see table 10, 4th data row. For (b), α_s is extracted from 14 measurements of the 3-jet cross section normalised to 2-jet cross section, using only data points with k-factor below 2.5 for both the 3-jet and 2-jet cross sections, see table 10, 5th data row. Other details are given in the caption to Fig. 9.

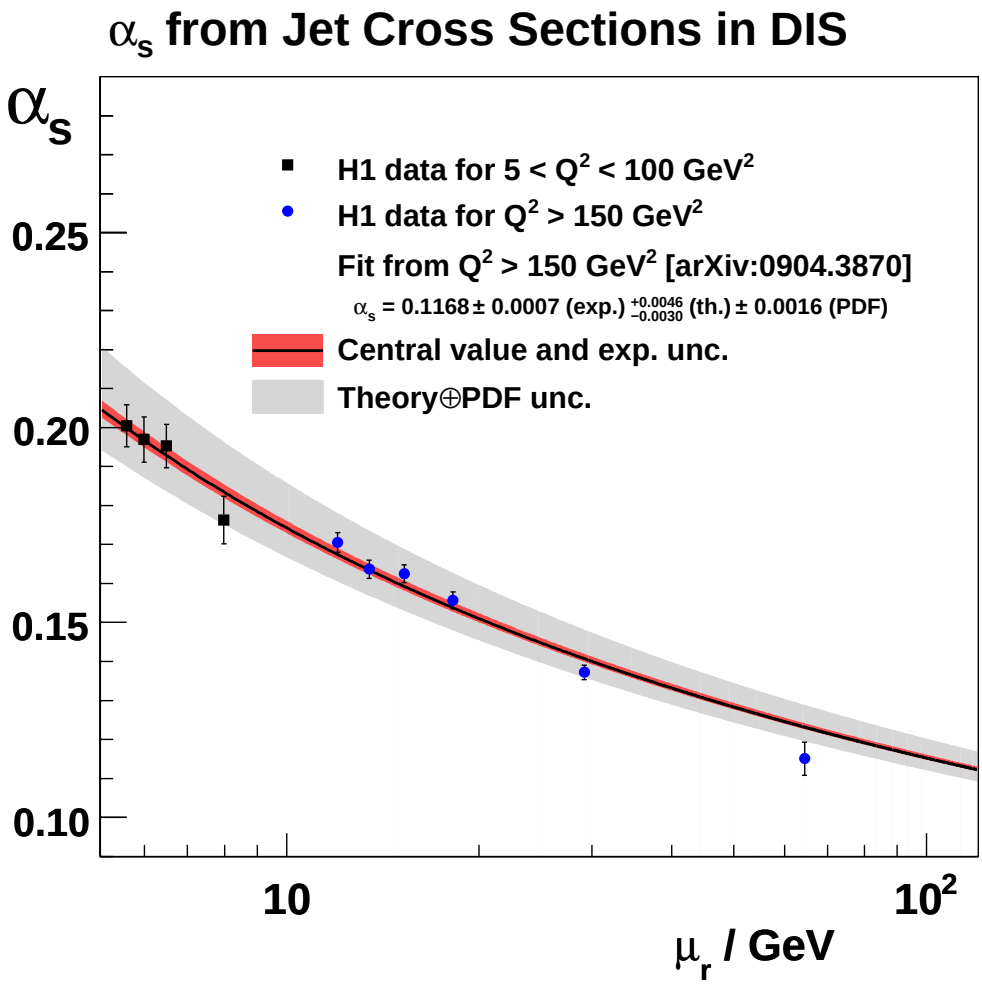

Figure 12: Values of $\alpha_s(\mu_r = \sqrt{(Q^2 + P^2_{T,\,\mathrm{obs}})/2})$ obtained by a simultaneous fit of all jet cross sections in each Q^2 bin of this analysis (squares) together with the fit in different bins at high Q^2 (circles) [4]. The solid line shows the two loop solution of the renormalisation group equation obtained by evolving the $\alpha_s(M_Z)$ extracted from jets at high Q^2. Other details are given in the caption to Fig. 9.